Rheol Acta (2009) 48:373–395
DOI 10.1007/s00397-008-0323-y

ORIGINAL CONTRIBUTION

Viscoelastic flow past confined objects using a micro–macro approach

R. O. Vargas · O. Manero · T. N. Phillips

Received: 16 May 2008 / Accepted: 28 August 2008 / Published online: 25 February 2009

Abstract This paper is concerned with the numerical prediction of viscoelastic flow past a cylinder in a channel and a sphere in a cylinder using molecular-based models. The basis of the numerical method employed is a micro–macro model in which the polymer dynamics is described by the evolution of an ensemble of Brownian configuration fields. The spectral element method is used to discretize the equations in space. Comparisons are made between the macroscopic simulations based on the Oldroyd B constitutive model and microscopic simulations based on Hookean dumbbells, and excellent agreement is found. The micro–macro approach can be used to simulate models, such as the finitely extensible nonlinear elastic (FENE) dumbbell model, which do not possess a closed-form constitutive equation. Numerical simulations are performed for the FENE model. The influence of the model parameters on the flow is described and, in particular, the dependence of the drag as a function of the Weissenberg number.

R. O. Vargas
Facultad de Química, Universidad Nacional Autónoma de México, Ciudad Universitaria 04510, Mexico D.F., Mexico
e-mail: reneosvargas@yahoo.com.mx

O. Manero
Instituto de Investigaciones en Materiales, Universidad Nacional Autónoma de México, Ciudad Universitaria 04510, Mexico D.F., Mexico
e-mail: manero@servidor.unam.mx

T. N. Phillips (✉)
School of Mathematics, Cardiff University, Cardiff CF24 4AG, UK
e-mail: phillipstn@cf.ac.uk

Keywords FENE model · Brownian configuration fields · Spectral element method · Flow past cylinder · Flow past sphere

Introduction

The significant improvements that have been made in the mathematical modelling of polymeric liquids over the last decade or so have necessitated a revolution in the development of computational techniques. This is because many models, such as the finitely extensible nonlinear elastic (FENE) dumbbell model, cannot be formulated in terms of closed-form constitutive equations. Therefore, many of the techniques that have been developed for solving differential or integral constitutive equations are not directly relevant or applicable to models based on kinetic theory, for example.

The traditional macroscopic approach to modelling, based on continuum fluid mechanics, in which the stress on a macroscopic fluid element is related to the deformation by a differential or integral constitutive equation is sufficient to provide a qualitative description of important flow phenomena in some situations for dilute polymer solutions. However, macroscopic models are unable to provide quantitative agreement with experimental observations in many complex flows of polymeric solutions. It should be noted that the situation for branched polymers is quite different, and macroscopic models such as the differential form of the pom-pom model (McLeish and Larson 1998) and the extended pom-pom model (Verbeeten et al. 2001, 2002), for example, have been successful in predicting the nonlinear behavior of materials in both shear and

extension simultaneously and in simulating complex flows of commercial polymer melts (Inkson et al. 2008).

Microscopic models, which utilize a coarse-grained description of polymer dynamics, provide the potential for computational rheologists to step nearer to the goal of delivering numerical solutions to complex flows of dilute polymeric solutions that are in quantitative agreement with experimental measurements and observations. In the microscopic approach, the polymer contribution to the extra stress is determined from the configuration of a large ensemble of model polymer molecules rather than from a constitutive equation.

The Fokker–Planck or diffusion equation (Bird et al. 1987), derived from considering a coarse-grained description of a polymer chain in terms of beads and springs, furnishes information about the configuration probability density function (pdf). However, numerical techniques for solving this equation are not always feasible, especially when the dimension of the configuration space is large. However, recent work has shown that the direct solution of the Fokker–Planck equation can be much more efficient than stochastic methods in the case of homogeneous flows, and moreover, complex flows can also be investigated (see Lozinski et al. 2003, for example).

Alternative approaches to the direct solution of the Fokker–Planck equation may be adopted. For example, by invoking a suitable closure approximation through a finite dimensional representation of the configuration pdf, one can derive a closed-form constitutive equation. Consistent closure schemes for statistical models of anisotropic fluids have been successfully developed and tested by Kröger et al. (2008). However, care should be exercised in deriving closure approximations since some of the most popular closure approximations are unable to reproduce the predicted behavior of the original kinetic theory model in certain flows (Sizaire et al. 1999). For example, we show in this paper that the FENE-P model, which is a closure approximation of the FENE model (Peterlin 1966), fails to provide an accurate representation of the original model for the complex flow past a cylinder in a channel. A more realistic closure approximation for FENE kinetic theory was developed by Lielens et al. (1999) using a two-parameter representation of the canonical radial distribution.

The idea of using stochastic simulations of the polymer dynamics to determine the polymeric contribution to the extra stress rather than solving closed-form constitutive equations was pioneered by Laso and Öttinger (1993) and further developed by Feigl et al. (1995) and Hua and Schieber (1998). The approach is very flexible and robust. Laso and Öttinger (1993) termed this hybrid method CONNFFESSIT. This is now one member of a broader class of numerical simulation methods known as micro–macro methods. The micro–macro approach in computational rheology combines a macroscopic description of the kinematics with a coarse-grained microscopic description of the evolution of the stress. The approach allows for greater flexibility in the kinetic theory models that can be used in numerical simulations since they do not require the existence of an equivalent or approximate closed-form constitutive equation. Furthermore, effects such as polydispersity and hydrodynamic interactions can be easily incorporated into these models since it is the motion of individual polymer molecules that is simulated.

The original CONNFFESSIT method suffered from several shortcomings, among which are the calculation of the trajectories of a large number of model polymer molecules and the possible generation of nonsmooth stresses. Variance reduction has been developed to reduce the statistical error in a stochastic simulation without increasing the number of trajectories that need to be simulated (Melchior and Öttinger 1995, 1996). These techniques have been implemented for kinetic theory models. The Brownian configuration field method of Hulsen et al. (1997) and Öttinger et al. (1997) and the Lagrangian particle method of Halin et al. (1998) belong to the second generation of micro–macro methods. They possess much improved numerical properties and are examples of variance-reduced stochastic simulation methods based on the idea of correlated local ensembles of model polymers. These are efficient micro–macro simulation techniques since they require the generation of fewer random numbers. Furthermore, these methods reduce the spatial fluctuations in the computed velocity and stress fields. These approaches, which are based on correlated Brownian forces, are suitable for problems in which physical fluctuations are unimportant.

In the micro–macro approach, the computation of the velocity and pressure is decoupled from the computation of the extra stress. This means that a symmetric positive-definite system for velocity and pressure is retained through the standard spectral element discretization of the mass and momentum equations. The polymeric contribution is determined using the method of Brownian configuration fields (Hulsen et al. 1997). The method is based on the evolution of a number of continuous Brownian configuration fields. Since these fields are spatially smooth, this approach is well-suited to a spectral element discretization, which is known to be efficient and accurate for smooth problems (Orszag 1980; Patera 1984). A numerical study is performed to investigate the use of a high-order spectral element

method in predicting the complex flow of a dilute solution past a cylinder in a channel and a sphere in a cylinder. The paper extends the work in Phillips and Smith (2006) to axisymmetric configurations and also provides a comprehensive set of results for the FENE model in these flow geometries.

Stochastic simulations based on Hookean dumbbells are compared with predictions obtained using the mathematically equivalent Oldroyd B constitutive equation in order to validate the algorithm. Excellent agreement is obtained as the number of configuration fields is increased. An extensive set of numerical results is presented for the flow of a FENE model fluid past a cylinder in a channel. The influence of the Weissenberg number, the Reynolds number, finite extensibility parameter and viscosity ratio on the drag, the stress along the center line and around the cylinder, and the streamlines is explored. It is also shown that the FENE-P model, which is a closure approximation of the FENE model, does not provide a good approximation in this flow configuration.

The paper is organized as follows: The macroscopic conservation equations and the coarse-grained microscopic model for of a polymer are presented. The temporal discretization of both the macroscopic and microscopic stages is described in the "Temporal discretization" section. The corresponding spatial discretization of these stages using the spectral element method is described in the "Spatial discretization" section. In the "Flow past a cylinder" section, numerical results are presented for the flow past a cylinder in a channel for the FENE and FENE-P dumbbell models in which the behavior of the drag, profiles of the stress components, and streamline patterns in terms of the material parameters are considered. In the "Flow past a sphere" section, we present the corresponding results for the flow of a FENE model fluid past a sphere in a cylinder. The main findings of the paper are summarized in the "Conclusions" section.

Governing equations for viscoelastic flows

The equations that govern the isothermal incompressible flow of a viscoelastic fluid comprise the conservation laws of mass and momentum together with an equation that relates the stress to the strain. The mathematical statements of the conservation laws of mass and momentum are

$$\nabla \cdot \mathbf{u} = 0 \tag{1}$$

$$\rho\left(\frac{\partial \mathbf{u}}{\partial t} + \mathbf{u}\cdot\nabla\mathbf{u}\right) = -\nabla p + \nabla\cdot\mathbf{T}, \tag{2}$$

respectively, where $\mathbf{u}$ is the velocity field, ρ is the density of the fluid, p is the pressure, and $\mathbf{T}$ is the extra-stress tensor. It is customary to express the extra-stress tensor of a polymeric solution as the sum of a solvent contribution, $2\eta_s\mathbf{d}$, and a polymeric contribution, $\boldsymbol{\tau}$, where η_s is the solvent viscosity and $\mathbf{d}$ is the rate-of-deformation tensor given by

$$\mathbf{d} = \frac{1}{2}(\nabla\mathbf{u} + (\nabla\mathbf{u})^T) \tag{3}$$

With this decomposition of the extra-stress tensor, the momentum equation becomes

$$\rho\left(\frac{\partial \mathbf{u}}{\partial t} + \mathbf{u}\cdot\nabla\mathbf{u}\right) = -\nabla p + \nabla\cdot\boldsymbol{\tau} + \eta_s\nabla^2\mathbf{u} \tag{4}$$

The polymeric contribution to the extra-stress tensor is determined using either a constitutive equation or stochastic simulations.

One of the models considered in this paper is the Oldroyd B model. This model can be derived from either continuum mechanics considerations or an equivalent microscopic description of the polymers dynamics in terms of an ensemble of Hookean dumbbells. The Oldroyd B constitutive model is

$$\boldsymbol{\tau} + \lambda\overset{\nabla}{\boldsymbol{\tau}} = 2\eta_p\mathbf{d}, \tag{5}$$

where λ is the relaxation time, η_p is the polymeric contribution to the viscosity, and the upper-convected derivative of $\boldsymbol{\tau}$ is defined by

$$\overset{\nabla}{\boldsymbol{\tau}} = \frac{\partial\boldsymbol{\tau}}{\partial t} + (\mathbf{u}\cdot\nabla)\boldsymbol{\tau} - \nabla\mathbf{u}\cdot\boldsymbol{\tau} - \boldsymbol{\tau}\cdot(\nabla\mathbf{u})^T \tag{6}$$

The governing equations Eqs. 1, 2, and 5 are made dimensionless by scaling length, velocity, and time by L, U, and L/U, respectively, and pressure and extra-stress tensor by $\eta_0 U/L$ where η_0 is the total zero-shear-rate viscosity given by $\eta_0 = \eta_s + \eta_p$. The dimensionless equations are

$$\nabla\cdot\mathbf{u} = 0 \tag{7}$$

$$\mathrm{Re}\left(\frac{\partial \mathbf{u}}{\partial t} + \mathbf{u}\cdot\nabla\mathbf{u}\right) = -\nabla p + \beta\nabla^2\mathbf{u} + \nabla\cdot\boldsymbol{\tau} \tag{8}$$

$$\boldsymbol{\tau} + \mathrm{We}\overset{\nabla}{\boldsymbol{\tau}} = 2(1-\beta)\mathbf{d}, \tag{9}$$

where the Reynolds number, Re; the Weissenberg number, We; and the viscosity ratio parameter, β, are defined by

$$\mathrm{Re} = \frac{\rho U L}{\eta_0}, \quad \mathrm{We} = \frac{\lambda U}{L}, \quad \beta = \frac{\eta_s}{\eta_0} \tag{10}$$

In this paper, polymer solutions are modelled as suspensions of elastic dumbbells comprising two identical

Brownian beads, with friction coefficient ζ, connected by an elastic spring. The polymer solution is considered to be sufficiently dilute so that the interaction between dumbbells may be ignored. The internal configuration of a dumbbell is given in terms of the end-to-end vector, $\mathbf{Q}$, connecting the two beads. This provides information about the orientation and length of the spring.

Taking into account the spring force, the viscous drag force, and the force due to Brownian motion, one can derive the equation of motion for the beads and, hence, the Fokker–Plank equation, which, for homogeneous flow, assumes the form

$$\frac{\partial \psi}{\partial t} = -\frac{\partial}{\partial \mathbf{Q}} \cdot \left\{ \left(\boldsymbol{\kappa}(t)\mathbf{Q} - \frac{2}{\zeta}\mathbf{F}(\mathbf{Q}) \right) \psi \right\} + \frac{2kT}{\zeta} \frac{\partial}{\partial \mathbf{Q}} \cdot \frac{\partial}{\partial \mathbf{Q}} \psi, \tag{11}$$

where $\boldsymbol{\kappa}$ is the velocity gradient, T is absolute temperature, k is Boltzmann's constant, and $\mathbf{F(Q)}$ is the spring force. The solution of Eq. 11 furnishes the probability $\psi(\mathbf{Q}, \mathbf{x}, t)d\mathbf{Q}$ of finding a dumbbell with configuration in the range $\mathbf{Q}$ to $\mathbf{Q} + d\mathbf{Q}$ at $(\mathbf{x}, t)$. Once the configuration pdf, ψ, is known, the polymer contribution to the extra-stress may be computed using the Kramers expression

$$\boldsymbol{\tau} = -nkT\mathbf{I} + n\langle \mathbf{Q} \otimes \mathbf{F(Q)} \rangle, \tag{12}$$

where n is the number of polymer molecules per unit volume, the symbol $\otimes$ denotes the outer product of two vectors, and the angular brackets denote the ensemble average over the configuration space. Note that the forms of the spring force considered (see Eqs. 13–15 below) ensure that the extra-stress tensor is symmetric.

Starting from the linear (Hookean) force law, given by

$$\mathbf{F}(\mathbf{Q}) = H\mathbf{Q}, \tag{13}$$

where H is the spring constant, one can derive the Oldroyd B model in which the relaxation time and the polymeric viscosity are given by

$$\lambda = \frac{\zeta}{4H}, \qquad \eta_p = nkT\lambda.$$

The linear spring force law (Eq. 13) is useful in situations where the dumbbells remain close to their equilibrium configuration. The problem with this expression is that at high flow rates and in extensional flow the dumbbells extend in length unboundedly, whereas real polymers can only be extended, at most, to their fully stretched length provided they do not break. The property of finite extensibility of the chains can be incorporated into a model by introducing a FENE spring force:

$$\mathbf{F}(\mathbf{Q}) = \frac{H\mathbf{Q}}{1 - (Q/Q_0)^2}, \tag{14}$$

where Q_0 is the maximum extension of each chain segment. There is no direct closure for the FENE model. If a closed-form constitutive equation is required, then a suitable approximation must be made. One such closure approximation for the FENE model is due to Peterlin (1966) and is based on a preaveraging of the spring force law in which the connector length in the denominator of Eq. 14 is replaced by an ensemble average, giving rise to the so-called FENE-P model

$$\mathbf{F}(\mathbf{Q}) = \frac{H\mathbf{Q}}{1 - (\langle Q \rangle / Q_0)^2}, \tag{15}$$

where $Q^2 = |\mathbf{Q}|^2$.

In principle, the Fokker–Planck equation (Eq. 11) may be solved for the configuration pdf of the polymer configuration at each position within the flow domain. This, in turn, can be used to determine the stress using the Kramers expression. However, this procedure is not always straightforward or computationally efficient, especially for multi-bead-spring models for representing polymer chains. Multi-bead-spring models possess a configuration space of large dimension. An alternative technique for generating the configuration distribution is to use the mathematical equivalence that exists, under certain conditions, between the Fokker–Planck equation and a stochastic differential equation (Öttinger 1996). However, since the stochastic approach does not furnish the configuration pdf, the extra stress cannot be evaluated using Eq. 12. Instead the extra stress is estimated by taking an average over a large number of realizations. This mathematical equivalence is an extremely important and powerful result since stochastic differential equations are generally more tractable numerically than the diffusion equation. The stochastic differential equation equivalent to Eq. 11 is

$$d\mathbf{Q}(t) = \left(\boldsymbol{\kappa}(t) \cdot \mathbf{Q} - \frac{2}{\zeta}\mathbf{F}(\mathbf{Q}) \right) + \sqrt{\frac{4kT}{\zeta}} d\mathbf{W}(t), \tag{16}$$

where $\mathbf{W}(t)$ is a multidimensional Wiener process. The components of $\mathbf{W}(t)$ are independent Wiener processes, i.e., Gaussian processes with zero mean and covariance $\langle \mathbf{W}(t)\mathbf{W}(t') \rangle = min(t, t')\mathbf{I}$. Physically, the intermolecular collisions are uncorrelated and, therefore, so are the Wiener processes at different points in space. However, the assumption of correlated Wiener processes is made in the development of many numerical stochastic simulation techniques including the

method of Brownian configuration fields considered here.

If we scale the length of the connector vector $\mathbf{Q}$ by $\sqrt{kT/H}$, the stochastic differential Eq. 16 becomes

$$d\mathbf{Q}(t) = \left(\boldsymbol{\kappa}(t)\cdot\mathbf{Q} - \frac{1}{2\lambda}\mathbf{F}(\mathbf{Q})\right) + \sqrt{\frac{1}{\lambda}}d\mathbf{W}(t). \tag{17}$$

In the method of Brownian configuration fields, the stochastic differential Eq. 17 is modified to account for the convection of the configuration field by the flow, so the evolution equation is

$$d\mathbf{Q}(t) = \left(-\mathbf{u}(x,t)\cdot\nabla\mathbf{Q}(x,t) + \boldsymbol{\kappa}(t)\cdot\mathbf{Q} - \frac{1}{2\lambda}\mathbf{F}(\mathrm{Q})\right) + \sqrt{\frac{1}{\lambda}}d\mathbf{W}(t). \tag{18}$$

Note that the spatial gradient of the configuration field is well-defined and smooth since, in this formulation, $d\mathbf{W}(t)$ only depends on the time and, therefore, influences the configuration field in a spatially uniform manner.

The Kramers expression for the polymer contribution to the extra-stress tensor becomes

$$\boldsymbol{\tau} = \frac{\eta_p}{\lambda}(-\mathbf{I} + \langle\mathbf{Q}\otimes\mathbf{F}(\mathrm{Q})\rangle) \tag{19}$$

for the Hookean and FENE dumbbell models. In the case of the FENE-P model, the Kramers expression Eq. 19 for the polymeric stress is multiplied by the factor $(b+d)/b$, where $b = HQ_0^2/kT$ is a dimensionless finite extensibility parameter and d is the dimension of the space.

For the planar flow past a cylinder, we assume, for the sake of simplicity, that the dumbbells lie in the plane of the flow, i.e., 2D dumbbell models are used for the purposes of our simulations. Although, this is not a physically reasonable assumption, it has been demonstrated (Chauvière and Lozinski 2008) that, in the case of the FENE dumbbells, the use of a 2D model does not significantly deteriorate the predictions of the polymer stress in shear flows. For the flow past a sphere, the 3D dumbbell model is used.

The Brownian configuration fields method (Hulsen et al. 1997) overcomes the problem of having to track particle trajectories, provides efficient variance reduction, and may be interpreted as an Eulerian implementation of the idea of correlated local ensembles. This method departs from the standard micro–macro approach in that it is based on the evolution of a number of configuration fields rather than the convection of discrete particles specified by their configuration vector. Dumbbell connectors with the same initial configuration and subject to the same random forces throughout the flow domain are combined to form a configuration field. The polymer dynamics is then described by the evolution of an ensemble of configuration fields instead of the evolution of local ensembles of model polymers. The method also provides a smooth spatial representation of the configuration field that can be differentiated to form the source term in the momentum equation.

An ensemble of N_f configuration fields $\mathbf{Q}_i(x,t)$, $i = 1, ..., N_f$, is introduced. Initially, these fields are spatially uniform and their values are independently sampled from the equilibrium distribution function of the dumbbell model. The evolution of each $\mathbf{Q}_i, i = 1, \ldots, N_f$ is governed by Eq. 18. This procedure for determining the polymeric contribution to the extra-stress tensor is equivalent to the tracking of individual model polymer molecules. At each point (x,t), an ensemble of configuration vectors is generated that experienced the same history in terms of the kinematics but which underwent different stochastic processes.

Temporal discretization

Most algorithms based on the micro–macro approach decouple the solution of the conservation laws from the solution of the evolution equation for the Brownian configuration fields within each time step. This is the only feasible strategy to adopt as far as micro–macro methods are concerned since the microscopic part of the calculation involves the evolution of an ensemble of configuration fields rather than the evolution of a constitutive equation for the extra-stress tensor. Typically, thousands rather than tens of configuration fields are used in the computations, thus ruling out a coupled or fully implicit solution procedure due to the constraints of computer memory. The coupling between the macroscopic and microscopic stages is achieved as follows. After the microscopic stage, the extra-stress tensor is evaluated by taking an arithmetic mean over the N_f configuration fields, and then, its divergence is computed and used to form the source term in the momentum equation. After the microscopic stage, the new velocity field is used to evolve the Brownian configuration fields forward in time over the next time step. In the macroscopic stage, all terms in the field equations are discretized implicitly except the divergence of the extra-stress tensor. In the microscopic stage, the stochastic differential equation for the configuration fields is discretized using second-order explicit schemes.

Macroscopic stage

The field equations are discretized in time using the first-order operator integration factor splitting scheme of Maday and Patera (1989) to discretize the convection term in the momentum equation. The semidiscrete approximation of the field equations is

$$\nabla \cdot \mathbf{u}^{n+1} = 0 \tag{20}$$

$$\frac{\mathrm{Re}}{\Delta t}\left(\mathbf{u}^{n+1} - \tilde{\mathbf{u}}\left(t^{n+1}\right)\right) = -\nabla p^{n+1} + \nabla \cdot \boldsymbol{\tau}^{n} + \beta \nabla^2 \mathbf{u}^{n+1}, \tag{21}$$

where $\tilde{\mathbf{u}}\left(t^{n+1}\right)$ is the solution at time $t = t^{n+1}$ of the pure convection problem:

$$\frac{\partial \tilde{\mathbf{u}}}{\partial t} = -\mathbf{u}^{n} \cdot \nabla \tilde{\mathbf{u}}, \quad t \in \left[t^{n}, t^{n+1}\right], \quad \text{with} \quad \tilde{\mathbf{u}}(x, t^{n}) = \mathbf{u}^{n}(x) \tag{22}$$

This initial value problem is solved using a fourth-order explicit Runge-Kutta (RK4) method. In the RK4 method, an additional time step, δt, is required where $\delta t = \Delta t / M$, where M is the number of RK4 iterations per outer time step and $\Delta t = t^{n+1} - t^{n}$.

Microscopic stage

The temporal discretization of the evolution equation for the configuration fields is performed using one of two second-order schemes with the choice of scheme dependent on the particular dumbbell model under consideration. An explicit predictor–corrector method is used in conjunction with the FENE-P model since the use of an implicit model is not practicable in this case due to the presence of the ensemble average in the denominator of the force law Eq. 15. In particular, the following predictor–corrector scheme is used in conjunction with the FENE-P model:

$$\bar{\mathbf{Q}}_i^{n+1} = \mathbf{Q}_i^{n} + \left[-\mathbf{u}^{n} \cdot \nabla \mathbf{Q}_i^{n} + \kappa \mathbf{Q}_i^{n} - \frac{1}{2\lambda}\mathbf{F}\left(\mathbf{Q}_i^{n}\right)\right]\Delta t + \sqrt{\frac{1}{\lambda}}\Delta \mathbf{W}_i^{n} \tag{23}$$

$$\begin{aligned}\mathbf{Q}_i^{n+1} = \mathbf{Q}_i^{n} &- \frac{1}{2}\left[\mathbf{u}^{n+1} \cdot \bar{\mathbf{Q}}_i^{n+1} + \mathbf{u}^{n} \cdot \mathbf{Q}_i^{n}\right]\Delta t \\ &+ \frac{1}{2}\left[\kappa^{n+1}\bar{\mathbf{Q}}_i^{n+1} + \kappa^{n}\mathbf{Q}_i^{n}\right]\Delta t \\ &- \frac{1}{4\lambda}\left[\mathbf{F}\left(\bar{\mathbf{Q}}_i^{n+1}\right) + \mathbf{F}(\mathbf{Q}_i^{n})\right]\Delta t + \sqrt{\frac{1}{\lambda}}\Delta \mathbf{W}_i^{n}\end{aligned} \tag{24}$$

The polymeric contribution to the extra-stress tensor at the new time level t^{n+1} is then computed using.

$$\boldsymbol{\tau}^{n+1} = \frac{\eta_p}{\lambda}\left(\frac{b+d}{b}\right)\left(-\mathbf{I} + \frac{1}{N_f}\sum_{i=1}^{N_f}\mathbf{Q}_i^{n+1} \otimes \mathbf{F}\left(\mathbf{Q}_i^{n+1}\right)\right) \tag{25}$$

There is, however, a serious problem associated with the use of explicit schemes such as the predictor–corrector method (Eqs. 23 and 24) for FENE-type models in that, for any finite time step, Δt, the scheme may produce a spring extension that exceeds the maximum prescribed by the model. Öttinger (1996) suggested two solutions to this problem. In the first approach, steps that result in an extension that is very close to the maximum allowable extension are rejected. The step is then repeated with a smaller time step. The second solution to the problem, which applies to the FENE model, completely avoids the possibility of predicting unphysical configurations by using an implicit algorithm. The implicit algorithm is similar in form to the predictor–corrector algorithm (Eqs. 23 and 24) except that the spring force law is treated implicitly in the corrector stage. Thus, we have the implicit scheme:

$$\bar{\mathbf{Q}}_i^{n+1} = \mathbf{Q}_i^{n} + \left(-\mathbf{u}^{n} \cdot \nabla \mathbf{Q}_i^{n} + \kappa^{n}\mathbf{Q}_i^{n} - \frac{1}{2\lambda}\frac{\mathbf{Q}_i^{n}}{\left[1 - (\mathbf{Q}_i^{n})^2/b\right]}\right)\Delta t + \sqrt{\frac{1}{\lambda}}\Delta \mathbf{W}_i^{n}, \tag{26}$$

$$\begin{aligned}&\left(1 + \frac{1}{4\lambda}\frac{\Delta t}{\left[1 - \left(\mathbf{Q}_i^{n+1}\right)^2/b\right]}\right)\mathbf{Q}_i^{n+1} \\ &\quad = \mathbf{Q}_i^{n} - \frac{1}{2}\left[\mathbf{u}^{n+1} \cdot \bar{\mathbf{Q}}_i^{n+1} + \mathbf{u}^{n} \cdot \mathbf{Q}_i^{n}\right]\Delta t \\ &\qquad + \frac{1}{2}\left[\kappa^{n+1}\bar{\mathbf{Q}}_i^{n+1} + \kappa^{n}\mathbf{Q}_i^{n}\right]\Delta t \\ &\qquad - \frac{1}{4\lambda}\frac{\mathbf{Q}_i^{n}}{\left[1 - (\mathbf{Q}_i^{n})^2/b\right]}\Delta t + \sqrt{\frac{1}{\lambda}}\Delta \mathbf{W}_i^{n}.\end{aligned} \tag{27}$$

The orientation of the dumbbell, $\mathbf{Q}_i^{n+1}$, is given by the right-hand side of Eq. 27, while its extension is determined from the solution of a cubic equation for $\mathbf{Q}_i^{n+1}$ formed from Eq. 27. Öttinger (1996) has shown that there is a unique solution of this cubic equation lying in $[0, \sqrt{b}]$. In the case of the FENE model, the polymeric contribution to the extra stress is computed using a expression similar to that in Eq. 25, except that $b + d$ is replaced by $b + d + 2$. Note that it is not computationally feasible to apply the implicit scheme

(Eqs. 26–27) to the FENE-P model for the reason given earlier, i.e., that related to the ensemble average of the configuration fields in the spring force law (Eq. 15).

Initial conditions

Initially, we require an equilibrium distribution for the configuration fields at time $t = 0$. At equilibrium, the polymeric contribution to the extra-stress tensor, $\boldsymbol{\tau}$, should be zero. This choice corresponds to a zero velocity field. From the definition of $\boldsymbol{\tau}$ in terms of the ensemble average (Eq. 19), the equilibrium distribution, ψ^{eq}, must satisfy

$$\int_{R^d} \mathbf{Q} \otimes \mathbf{F}(\mathbf{Q}) \psi^{eq}(\mathbf{Q}) d\mathbf{Q} = \mathbf{I}, \tag{28}$$

where the integral is over configuration space. For the Hookean dumbbell model, the equilibrium distribution function is a Gaussian distribution with zero mean and unit covariance matrix. For the FENE-P model, the initial configuration fields are generated using the equilibrium distribution function for the FENE-P model (Keunings 1997), which is, again, a Gaussian distribution with zero mean, but this time, the covariance matrix is $b/(b + d)$ times the unit matrix. Initially, the fluid is assumed to be at rest, so that $\mathbf{u}^{(0)} = \mathbf{0}$.

Spatial discretization

The spectral element method is used to discretize both stages of the numerical method in space. The physical domain Ω is partitioned into K nonoverlapping spectral elements Ω_k, $1 \le k \le K$, such that $\bigcup_{k=1}^{K} \Omega_k = \Omega$. We denote by $\mathbf{P}_N(\Omega_k)$ the space of all polynomials on Ω_k of degree $\le N$, and further define

$$P_N(\Omega) = \{\phi : \phi|_{\Omega_k} \in \mathbf{P}_N(\Omega_k)\} \tag{29}$$

Each of the spectral elements is mapped onto a parent element $D = [-1, 1] \times [-1, 1]$, where each point $(\xi, \eta) \in D$ is associated with a point $(x(\xi, \eta))$, $(y(\xi, \eta)) \in \Omega_k$ by the transfinite mapping technique of Gordon and Hall (1973). The dependent variables are approximated on D using Lagrangian interpolants of degree N in both spatial directions, based on the Gauss–Lobatto–Legendre (GLL) points. This creates a GLL grid inside the spectral elements.

Macroscopic stage

The spectral element method is applied to the weak formulation of the semidiscrete equations (Eqs. 20 and 21). Suitable function spaces are chosen for the dependent variables. The choice of function spaces is based on theoretical considerations of the three-field Stokes problem in the absence of any corresponding theory for the viscoelastic problem. The velocity is chosen to be in a subspace, V, of $[H^1(\Omega)]^2$, whose elements satisfy the prescribed velocity boundary conditions. The approximate spaces for pressure and stress for this generalized Stokes problem are

$$P = \left[L^2(\Omega)\right], \tag{30}$$

$$T = \left[L^2(\Omega)\right]_s^4, \tag{31}$$

where the subscript s denotes the space of symmetric tensors. For this choice of function spaces, Gerritsma and Phillips (2000) have shown that this choice results in a well-posed problem for the corresponding Stokes problem.

The weak formulation of Eqs. 20 and 21 is the following: find $(\mathbf{u}^{n+1}, p^{n+1}) \in V \times P$, such that

$$d\left(\mathbf{u}^{n+1}, q\right) = 0, \quad \forall q \in P, \tag{32}$$

$$\beta a\left(\mathbf{u}^{n+1}, \mathbf{v}\right) + \frac{\mathrm{Re}}{\Delta t} b\left(\mathbf{u}^{n+1}, \mathbf{v}\right) - d^*\left(p^{n+1}, \mathbf{v}\right) = -c\left(\boldsymbol{\tau}^n, \mathbf{v}\right) + \left(\mathbf{g}^n, \mathbf{v}\right) \quad \forall \mathbf{v} \in V, \tag{33}$$

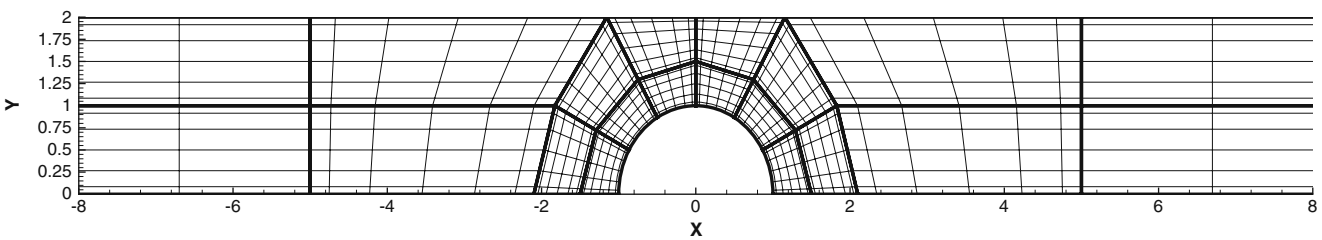

Fig. 1 Spectral element mesh with $K = 20$ and $N = 6$

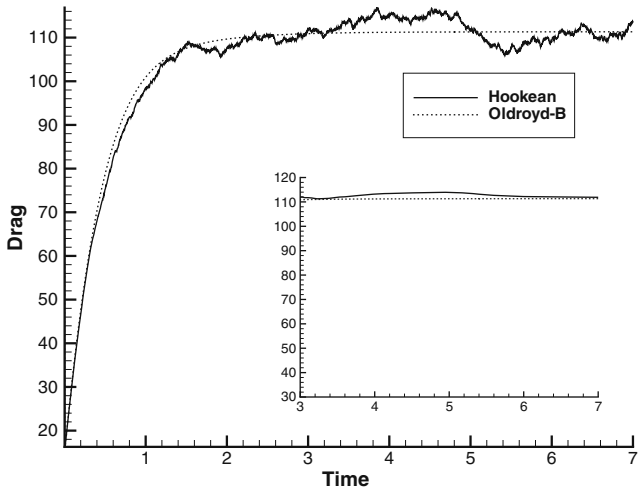

Fig. 2 Comparison of the dimensionless drag on the cylinder using the Oldroyd-B and Hookean dumbbell models for We = 0.6, Re = 0.01, and $\beta = 1/9$, with $N = 6$. For the Hookean dumbbell model, $N_f = 2{,}000$. *Inset*: evolution of the time-averaged (from $t = 3$) dimensionless drag

where the bilinear forms $a(\cdot,\cdot)$, $b(\cdot,\cdot)$, $c(\cdot,\cdot)$, and $d(\cdot,\cdot)$ are defined by

$$a(\mathbf{u},\mathbf{v}) = \int_\Omega \nabla\mathbf{u} : \nabla\mathbf{v} d\Omega,$$

$$b(\mathbf{u},\mathbf{v}) = \int_\Omega \mathbf{u}\cdot\mathbf{v} d\Omega,$$

$$c(\boldsymbol{\tau},\mathbf{v}) = \int_\Omega \boldsymbol{\tau} : \nabla\mathbf{v} d\Omega,$$

$$d(\mathbf{u},q) = \int_\Omega \nabla\cdot\mathbf{u} q d\Omega,$$

and $\mathbf{g}^n = \frac{\mathrm{Re}}{\Delta t}\widetilde{\mathbf{u}}\left(t^{n+1}\right)$. The bilinear forms $a(\cdot,\cdot)$, $b(\cdot,\cdot)$, $c(\cdot,\cdot)$ and $d(\cdot,\cdot)$ induce continuous linear operators $A : V \longrightarrow V'$, $B : V \longrightarrow V'$, $C : T \longrightarrow V'$ and $D : V \longrightarrow P'$ defined by

$$[A\mathbf{u},\mathbf{v}] = a(\mathbf{u},\mathbf{v}), \quad \forall\mathbf{u},\mathbf{v}\in V,$$

$$[B\mathbf{u},\mathbf{v}] = b(\mathbf{u},\mathbf{v}), \quad \forall\mathbf{u},\mathbf{v}\in V,$$

$$[C\boldsymbol{\tau},\mathbf{v}] = c(\boldsymbol{\tau},\mathbf{v}), \quad \forall\boldsymbol{\tau}\in\tau,$$

$$[D\mathbf{u},q] = d(\mathbf{u},q), \quad \forall\mathbf{u}\in V, \quad \forall q\in P,$$

$$[D^*p,\mathbf{v}] = d^*(p,\mathbf{v}), \quad \forall p\in P, \quad \forall\mathbf{v}\in V,$$

In this notation, the dual problem to Eqs. 32 and 33 is

$$D\mathbf{u}^{n+1} = 0 \tag{34}$$

$$\left[\beta A + \left(\frac{\mathrm{Re}}{\Delta t}\right)B\right]\mathbf{u}^{n+1} - D^*p^{n+1} = -C\boldsymbol{\tau}^n + \mathbf{g}^n. \tag{35}$$

The discrete approximation spaces must satisfy a compatibility condition, known as the LBB condition, to ensure that the problem is well-posed. For spectral elements, (Maday and Patera 1989) have shown that the LBB condition is satisfied when the velocity approximation space is the polynomial space $\mathbf{P}_N(\Omega)$ and the pressure approximation space is $\mathbf{P}_{N-2}(\Omega)$. A Gauss–

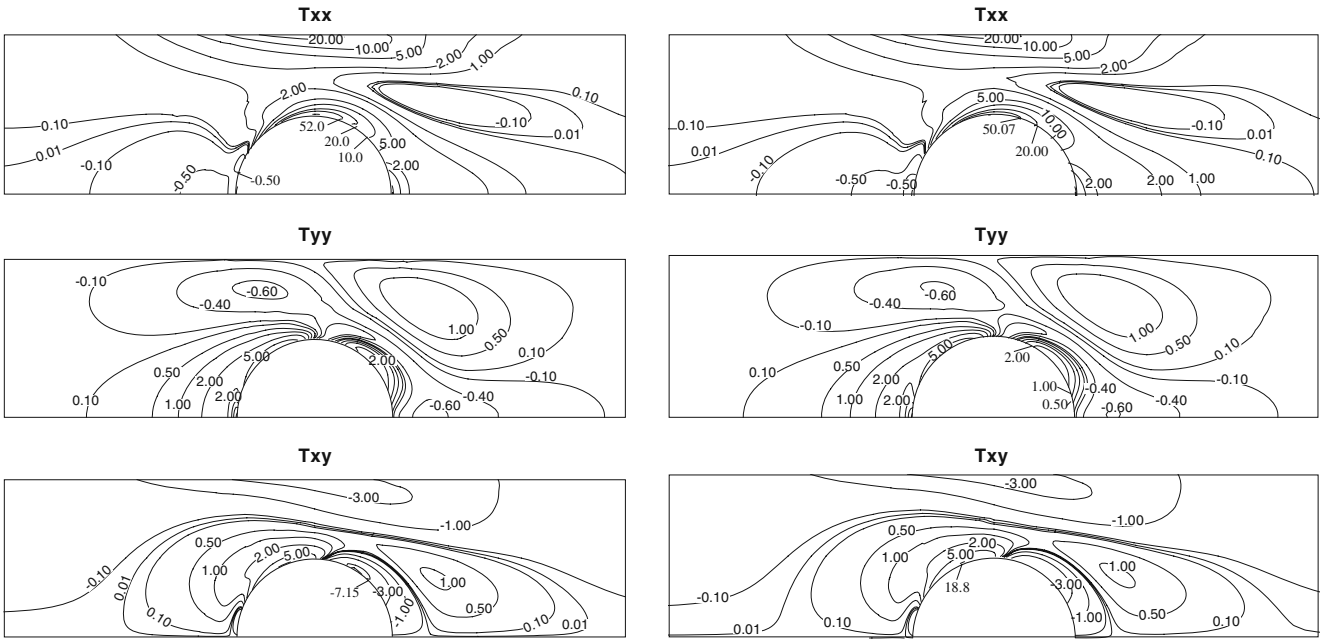

Fig. 3 Comparison of contour plots of the stress components generated using the Oldroyd-B model (*left-hand side*) and the Hookean dumbbell model (*right-hand side*) for We = 0.6, Re = 0.01, and $\beta = 1/9$, with $N = 6$. For the Hookean dumbbell model $N_f = 2{,}000$

Lobatto quadrature rule will be used to integrate the velocities, whereas a Gauss quadrature rule integrates the pressure. The stress is approximated by polynomials in the space $\mathbf{P}_N(\Omega)$ as well, with the difference being that the stress components are allowed to be discontinuous across the element boundaries. Gerritsma and Phillips (2000) have shown that this is a sufficient condition for stability of the corresponding three-field Stokes problem. The velocity and stress representations are given by

$$\mathbf{u}_N^k(\xi,\eta) = \sum_{i=0}^{N}\sum_{j=0}^{N} \mathbf{u}_{i,j}^k h_i(\xi) h_j(\eta) \tag{36}$$

$$\boldsymbol{\tau}_N^k(\xi,\eta) = \sum_{i=0}^{N}\sum_{j=0}^{N} \boldsymbol{\tau}_{i,j}^k h_i(\xi) h_j(\eta), \tag{37}$$

where the Lagrangian interpolants $h_i(\xi)$ are defined by

$$h_i(\xi) = -\frac{(1-\xi^2)L'_N(\xi)}{N(N+1)L_N(\xi_i)(\xi-\xi_i)}, \quad 0 \le i \le N. \tag{38}$$

The pressure representation is

$$p_N^k(\xi,\eta) = \sum_{i=1}^{N-1}\sum_{j=1}^{N-1} p_{i,j}^k \widetilde{h}_i(\xi)\widetilde{h}_j(\eta), \tag{39}$$

in which the Lagrangian interpolants are

$$\widetilde{h}_i(\xi) = -\frac{(1-\xi_i^2)L'_N(\xi)}{N(N+1)L_N(\xi_i)(\xi-\xi_i)}, \quad 1 \le i \le N-1. \tag{40}$$

The spectral element discretization of the dual problem (Eqs. 34 and 35) results in the following discrete

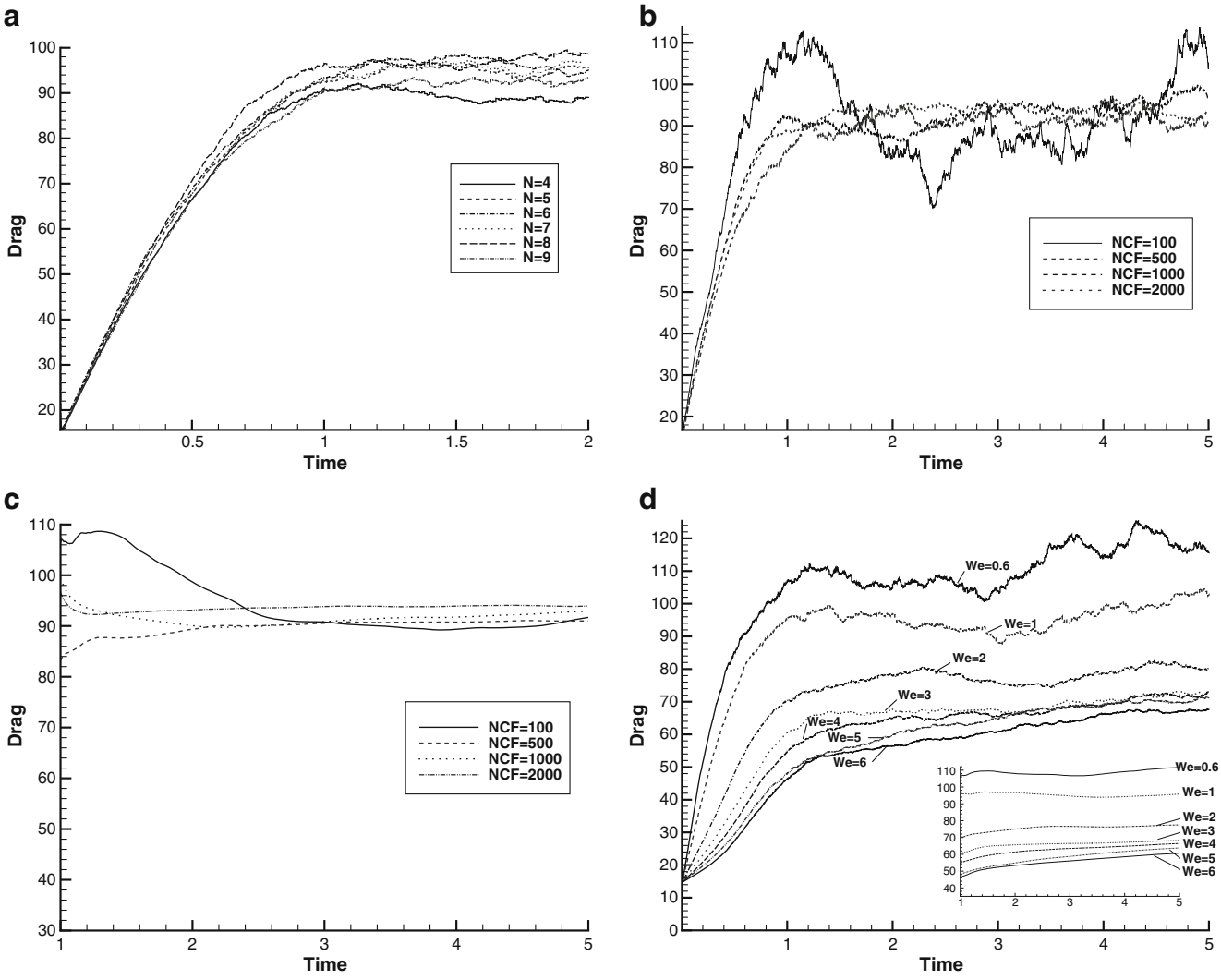

Fig. 4 Dependence of the evolution of the drag on **a** mesh refinement, **b** number of configuration fields, **c** number of configuration fields in a time-averaged sense (from $t = 1$), and **d** Weissenberg number (*inset*: evolution of the time-averaged (from $t = 1$) dimensionless drag), for the FENE dumbbell model with default values We = 1, Re = 0.01, $\beta = 1/9$, $b = 50$, $N = 6$, and $N_f = 2{,}000$

Table 1 Steady state drag on the cylinder surface as a function of Weissenberg number

We	Drag
0.6	107.6528
1.0	96.4207
2.0	77.8543
3.0	74.9829
4.0	70.7530
5.0	64.3565
6.0	65.8450

problem:

$$D_N \mathbf{u}_N^{n+1} = 0 \tag{41}$$

$$\left[\beta A_N + \left(\frac{\mathrm{Re}}{\Delta t}\right) B_N\right] \mathbf{u}_N^{n+1} - D_N^* \mathbf{p}_N^{n+1} = -C_N \boldsymbol{\tau}_N^n + \mathbf{g}_N^n, \tag{42}$$

where D_N and C_N are the discrete divergence operators acting on the velocity and stress, respectively, and D_N^T is the gradient operator acting on pressure, A_N is the discrete Laplace operator, B_N is the discrete velocity mass matrix, and g_N denotes the discrete form of the right-hand side of Eq. 35. Eliminating the velocity using the discrete continuity equation yields the pressure equation:

$$D_N H_N^{-1} D_N^T \mathbf{p}_N^{n+1} = -D_N H_N^{-1} \left(\mathbf{g}_N - C_N \boldsymbol{\tau}_N^n\right), \tag{43}$$

where

$$H_N = \beta A_N + \frac{\mathrm{Re}}{\Delta t} B_N \tag{44}$$

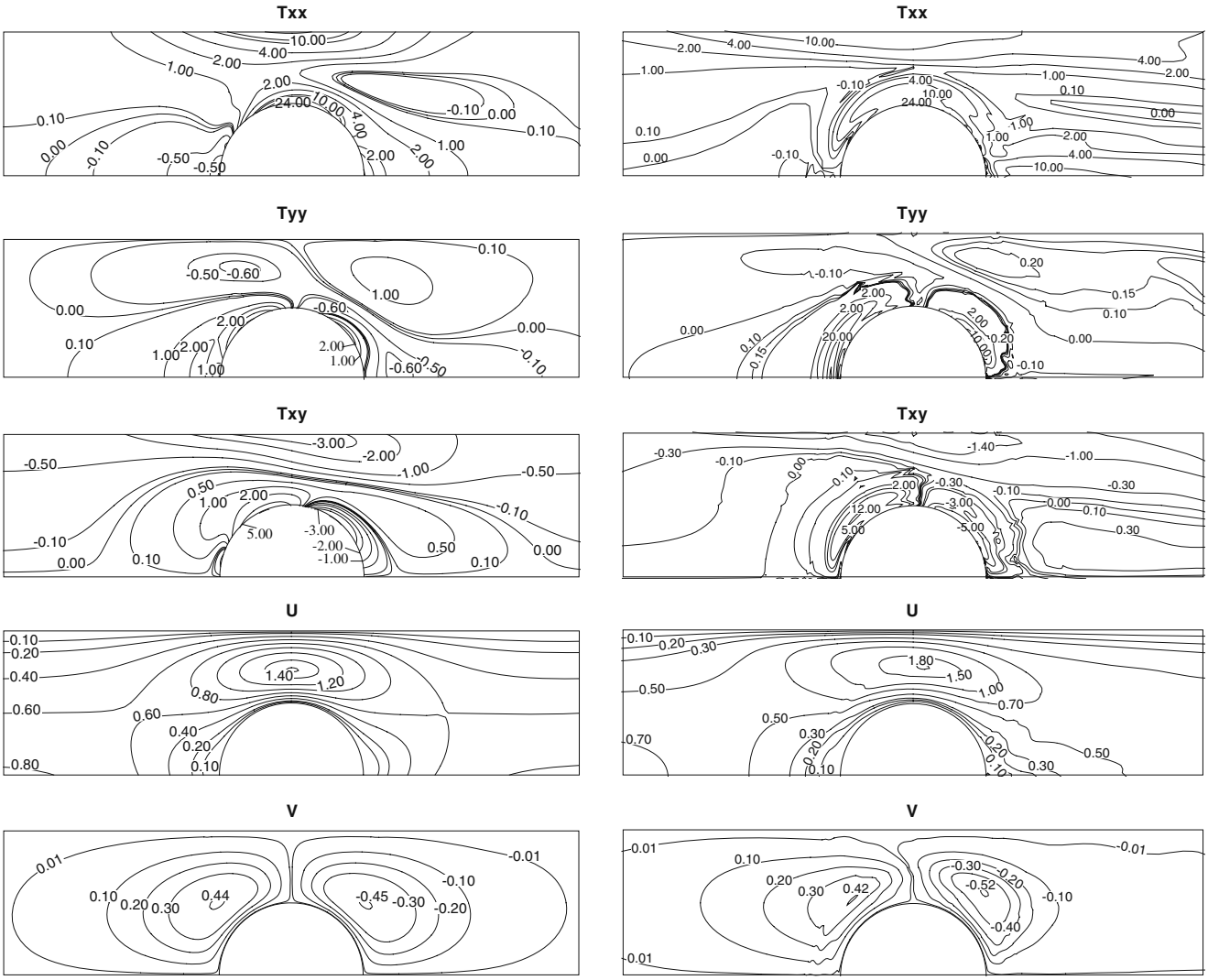

Fig. 5 Comparison of contour plots of the stress and velocity components generated using the FENE model for We = 0.6 (*left*) and We = 5 (*right*) for Re = 0.01, $\beta = 1/9$, and $b = 50$ with $N_f = 2{,}000$, and $N = 6$

is a discrete Helmholtz-like operator. The operator $U_N = D_N H_N^{-1} D_N^T$ is known as the Uzawa operator. Simplified, the pressure equation may be written as

$$U_N \mathbf{p}_N^{n+1} = \mathbf{b}_N, \tag{45}$$

where $\mathbf{b}_N$ is the right-hand side of Eq. 42.

To solve the pressure equation (Eq. 45), a nested preconditioned conjugate gradient (PCG) algorithm is used. The solution of the pressure requires a nested solver since both the Uzawa operator $U = DH^{-1}D^T$ and the Helmholtz operator H need to be inverted. Since both operators are symmetric, the PCG method can be used. The inversion of the Helmholtz operator is nested within the inversion of the Uzawa operator. The Schur complement method has been used to reduce the size of the Helmholtz operator. This method eliminates the interior degrees of freedom associated with each spectral element to leave a system that serves to determine the unknowns at element interfaces. The Schur complement is stored in an LU decomposition and used as a preconditioner for the conjugate gradient method.

The preconditioner that was found to be the most efficient for the Uzawa operator is based on the finite element mesh comprised of the inner GLL nodes of each spectral element. The mesh is triangulated with no overlapping nodes. This preconditioner is based on the finite element mass and stiffness matrices on the local finite elements, which are M_k^{FE} and E_k^{FE}, and it is given as:

$$P_U^{-1} = \mathrm{FE}_U^{-1} = \sum_{k=1}^{K} R_k^T \left(\frac{M_k^{\mathrm{FE}}}{\beta} + M_l E_k^{\mathrm{FE}} \right)^{-1} R_k, \tag{46}$$

where R_k is the restriction operator, which maps a global vector to a vector of length equal to the number of GLL nodes of the spectral element. The preconditioner is stored as an LU decomposition.

Microscopic stage

The semidiscrete stochastic differential equations (Eqs. 23 and 24 or Eqs. 26 and 27) are discretized in space using the discontinuous Galerkin (DG) method. The DG approach is efficient since it circumvents the need to solve a large coupled system of equations of the order of the total number of mesh points in the domain Ω. Instead, the DG method requires the solution of smaller problems defined over each spectral element. The appropriate function space for the configuration fields is $\mathcal{Q} = (L^2(\Omega))^d$. The DG method is constructed by multiplying Eq. 24 or Eq. 27 by a test function $S \in \mathcal{Q}$ and integrating over a spectral element Ω_k. The convection term is integrated by parts twice. In the forward step, the condition $\mathbf{Q} = \mathbf{Q}^{in}$ is applied weakly along inflow portions, γ^{in}, of Ω_k. The inflow portion of the boundary is characterized by the condition $\mathbf{u} \cdot \mathbf{n} < 0$ and $\mathbf{Q}^{in}$ is the value of $\mathbf{Q}$ in the neighboring upwind spectral element or the prescribed condition at the inflow to the domain and $\mathbf{n}$ is the unit outward normal to the boundary of Ω_k. In the backward step, the new boundary terms are left unchanged. Therefore, in the weak formulation of Eq. 24 or Eq. 27 over each spectral element Ω_k, terms of the form $(\mathbf{u}^n \cdot \nabla \mathbf{Q}_i, S)_{\Omega_k}$ are replaced by

$$\left(\mathbf{u}^n \cdot \nabla \mathbf{Q}_i, S\right)_{\Omega_k} + \left(\mathbf{u}^n \cdot \mathbf{u}(\mathbf{Q}_i^{in} - \mathbf{Q}_i), S\right)_{\gamma^{in}} \tag{47}$$

for $i = 1, \ldots, N_f$. The spatial discretization of the configuration fields is performed using discontinuous approximations in $P_N(\Omega)$. When $N = 6$, the microscopic part of the calculation accounts for about 70% of the CPU time.

Flow past a cylinder

The complex problem of flow past a cylinder placed symmetrically in a channel is considered in this section. The aspect or blockage ratio is defined to be $\Lambda = \frac{R}{H}$, where R is the radius of the cylinder and H is the half-width of the channel. In this paper, we consider the 50% blockage case, i.e., $\Lambda = 0.5$. This value has been chosen consistently as one of the benchmark problems in this field. The cylinder benchmark problem

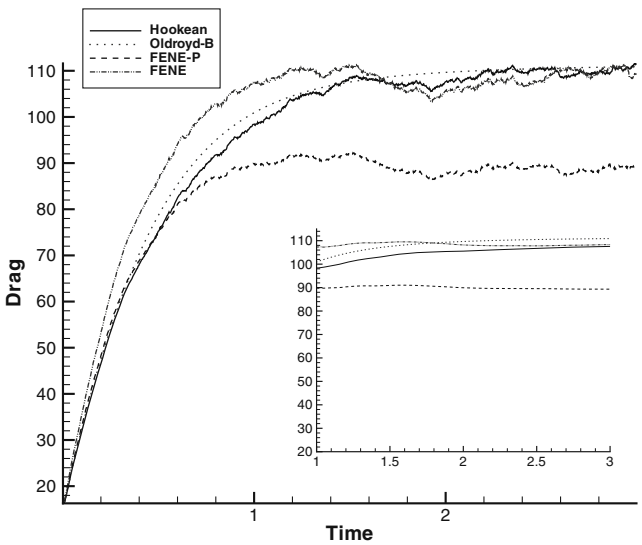

Fig. 6 Comparison of the evolution of the drag for the Hookean, FENE, and FENE-P dumbbell models with We = 0.6, Re = 0.01, $\beta = 1/9$, and $b = 50$ for $N = 6$ and $N_f = 2{,}000$. *Inset*: evolution of the time-averaged (from $t = 1$) dimensionless drag

is acknowledged to be more difficult than the related sphere problem because, for the same aspect ratio Λ, the planar flow past a cylinder undergoes a stronger contraction and expansion than the axisymmetric flow past a sphere. The computational domain extends a distance 25 units upstream and 25 units downstream of the cylinder, so that the assumption of fully developed flow conditions at entry and exit is valid. A comprehensive discussion of these problems (flow past a cylinder and sphere) can be found in the monograph of Owens and Phillips (2002).

A typical spectral element mesh for this problem is shown in Fig. 1. In this particular mesh, the number of spectral elements is $K = 20$ and the order of the spectral approximation is $N = 6$. The time step is chosen to be $\triangle t = 2 \times 10^{-3}$. The pure convection problems are solved with eight inner time steps per outer time step, i.e., $M = 8$.

Although the dimensionless drag coefficient is often used in the literature as a measure for testing the accuracy of numerical approximations to the solution of flow past a cylinder by comparing predictions with

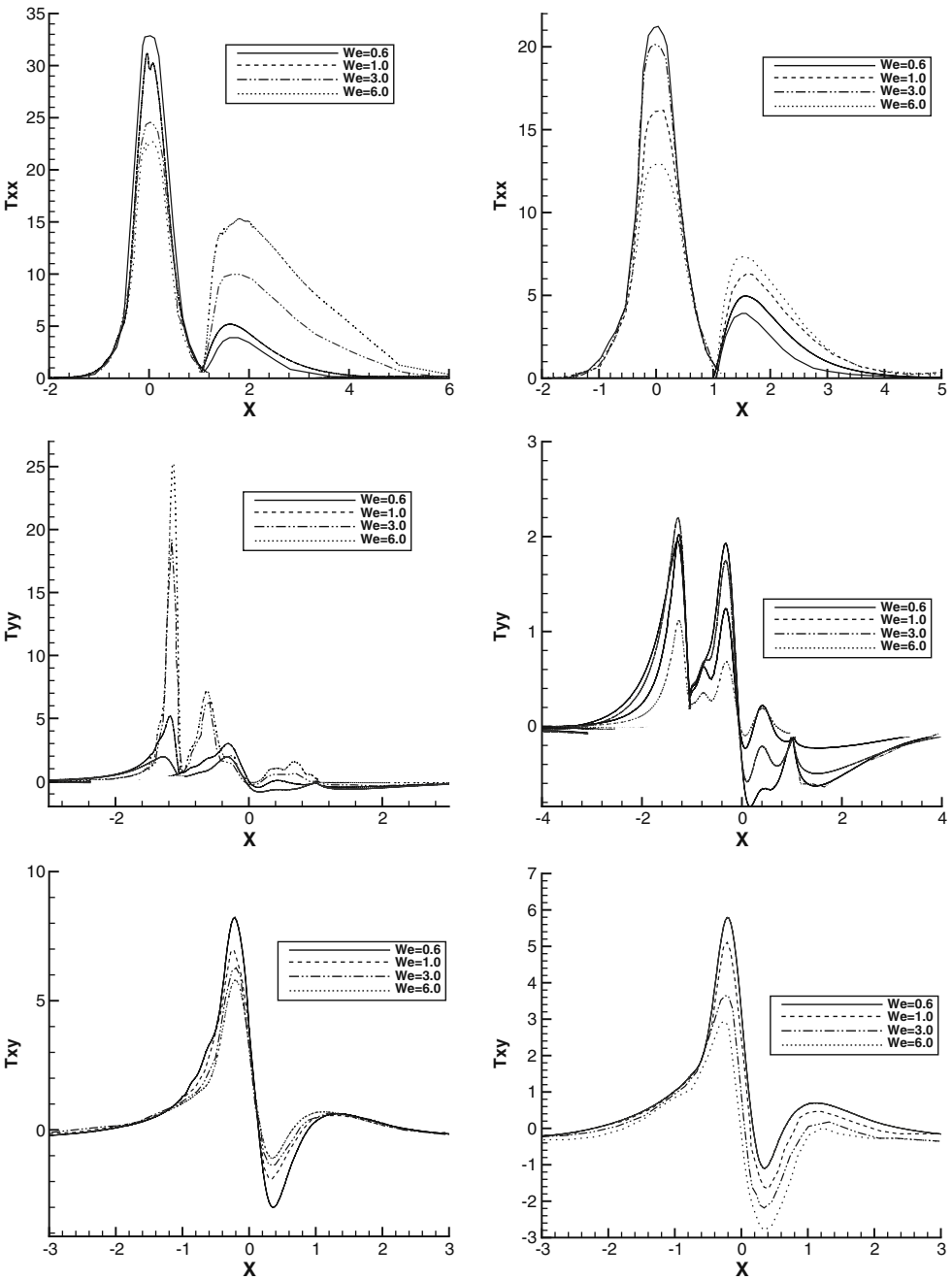

Fig. 7 Comparison of the dependence of the profiles of the polymeric stress components along the axis of symmetry line ($y = 0$) and around the cylinder on the Weissenberg number for the FENE model (*left*) and FENE-P model (*right*) with $\mathrm{Re} = 0.01$, $\beta = 1/9$, and $b = 50$ for $N = 6$ and $N_f = 2{,}000$

other results in the literature, it may not be sensitive to inaccuracies in the stress components away from the cylinder surface. Therefore, it is important to examine the behavior of the stress components globally since numerical oscillations or other mesh-dependent features may be overseen by simply concentrating on the computation of the drag coefficient. The expression for the dimensionless drag on the cylinder is

$$F = 2\int_0^{\pi} \left\{ \left(-p + 2\beta \frac{\partial u}{\partial x} + \tau_{xx} \right) \cos\theta + \left(\beta \left(\frac{\partial v}{\partial x} + \frac{\partial u}{\partial y} \right) + \tau_{xy} \right) \sin\theta \right\} d\theta, \qquad (48)$$

where F has been made dimensionless with ηU.

The value of the drag in the Navier–Stokes problem is compared to a result generated by Hulsen et al. (1997). For the Reynolds number $\mathrm{Re} = 0.01$, Hulsen et al. (1997) calculated the drag to be $F = 132.3584$, which compares favorably with the value of $F = 132.3507$ calculated using our method. The two values agree to within 0.01% of each other.

Oldroyd B and Hookean dumbbell models

The first set of results compares macroscopic predictions using the Oldroyd B model with micro–macro predictions based on the evolution of Brownian configuration fields using Hookean dumbbells. This comparison is performed in order to validate the micro–macro approach since the Hookean dumbbell model is mathematically equivalent to the Oldroyd B model. A comparison of the evolution of the drag predicted by the two models is given in Fig. 2 for $\mathrm{We} = 0.6$ and $\mathrm{Re} = 0.01$. Very good agreement is obtained between the two approaches, particularly as steady state is reached, thereby confirming the validity of the micro–macro approach. In the inset of Fig. 2, we plot the evolution of the time-averaged value of the drag for $t \geq 3$, i.e., we plot the evolution of

$$\frac{1}{K+1} \sum_{k=K_0}^{K} \mathrm{drag}(k\Delta t), \qquad (49)$$

where K_0 is the smallest integer greater than or equal to $3/\Delta t$. The time-averaged values smooth out the

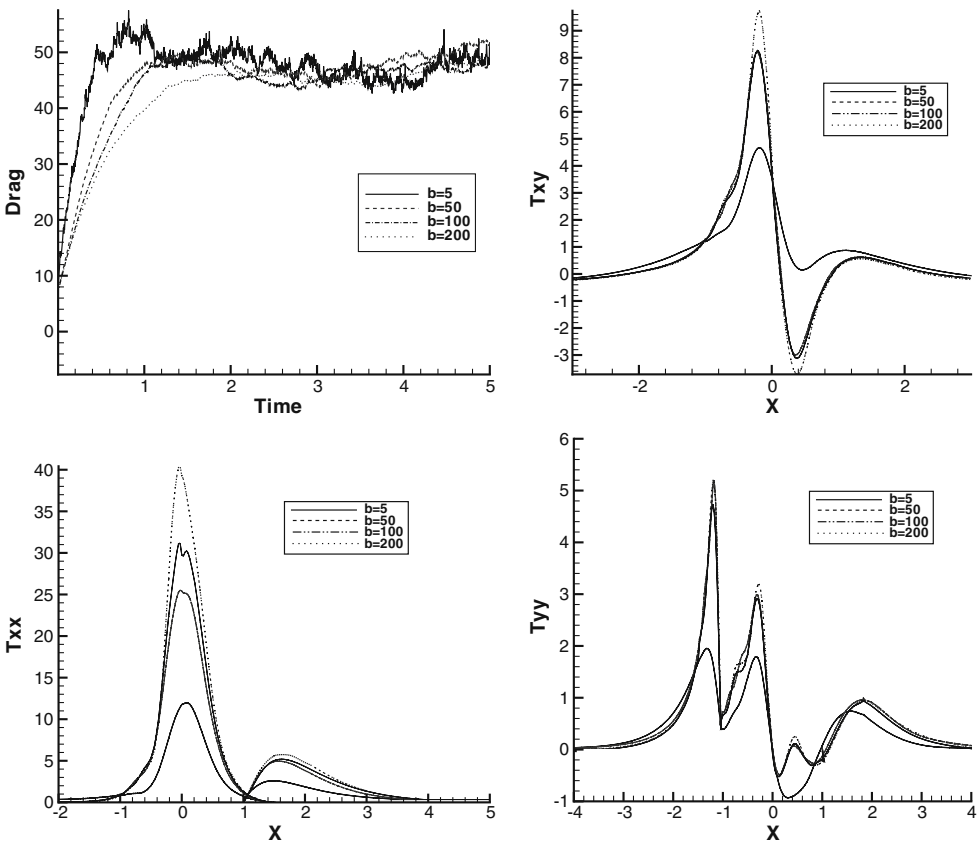

Fig. 8 Dependence of the drag and the polymeric extra-stress components along the center line on the finite extensibility parameter b for the FENE dumbbell model with $\mathrm{We} = 1$, $\mathrm{Re} = 0.01$, and $\beta = 1/9$ for $N = 6$ and $N_f = 2{,}000$

transient fluctuations in drag and clearly show the convergence of the drag for two models.

However, good agreement of the two approaches as far as the calculation of the drag is concerned should not be interpreted as meaning that the corresponding global fields are necessarily in close agreement as well. We demonstrate that the global fields are in agreement by comparing contours of the components of the extra-stress tensor generated by the macroscopic and micro–macro approaches. This comparison is shown in Fig. 3. Excellent quantitative agreement is obtained across the two approaches as evidenced by the fine-scale features predicted using both approaches and the location of contours of the same height.

FENE and FENE-P models

Our study of FENE models begins with a discussion of the influence of the discretization parameters on the evolution of the drag for We $= 1$, Re $= 0.01$, $\beta = 1/9$ and $b = 50$. In Fig. 4a, we present the evolution of the drag on the cylinder as a function of polynomial order, N, for the FENE model. The number of spectral elements remains constant in these simulations. These results demonstrate that mesh convergence is obtained as the order of the approximation is increased. Very little difference is observed in these predictions for $N > 4$ and, certainly as steady state is reached, the agreement is very good. The differences that exist can be explained by appealing to the noise in the stochastic simulations.

In Fig. 4b, we show the influence of the number configuration fields, N_f, on the evolution of the drag. Steadily increasing the number of configuration fields, $N_f = 100, 500, 1{,}000, 2{,}000$, reduces the temporal fluctuations in the drag as expected. Again, we see general improvement in the prediction of the drag with refinement in terms the microscopic part of the calculation, and there is very little difference when the number of configuration fields is doubled from 1,000 to 2,000. In Fig. 4c, we plot the evolution of the time-averaged value of the drag given by Eq. 49 for $t \geq 1$, where K_0 is now the smallest integer greater than or equal to $1/\Delta t$. The time-averaged values clearly show the convergence of the drag as the number of configuration fields is increased.

The dependence of the evolution of the drag on the cylinder on the Weissenberg number is shown in Fig. 4d for Re $= 0.01$, $\beta = 1/9$, and $b = 50$. Note that the fluctuations in the evolution of the drag decrease with increasing elasticity. This is due to the

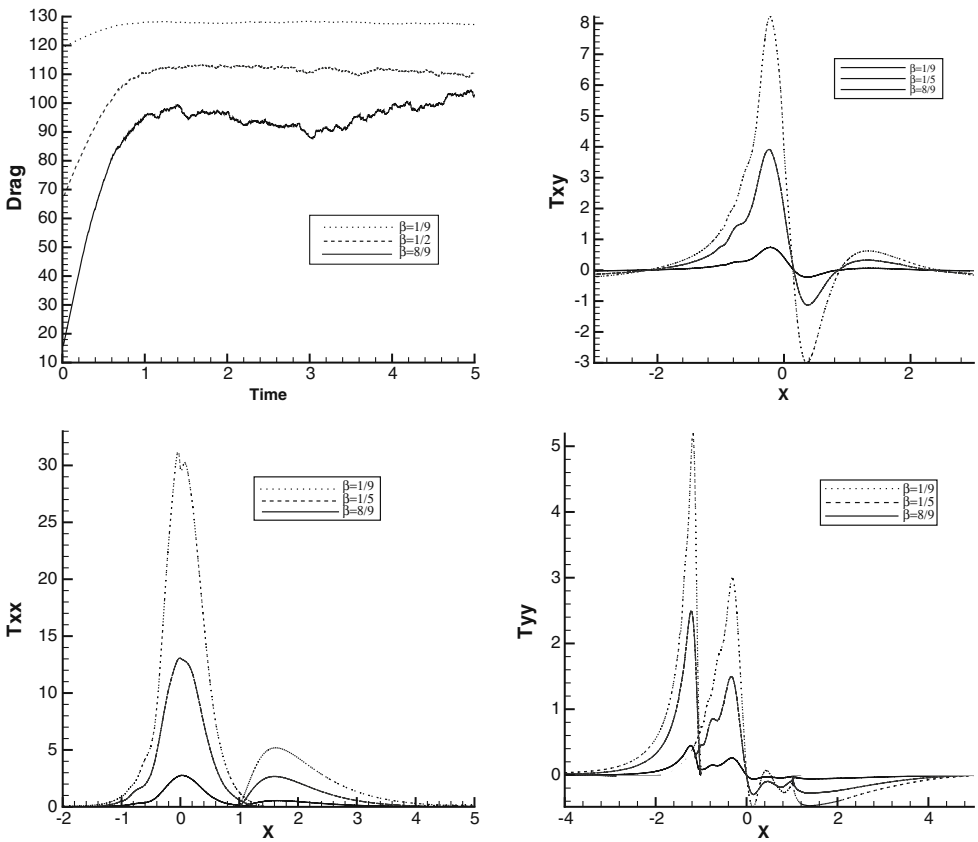

Fig. 9 Dependence of the drag and the polymeric extra-stress components along the center line on the viscosity ratio β for the FENE dumbbell model with We $= 1$, Re $= 0.01$, and $b = 50$ for $N = 6$ and $N_f = 2{,}000$

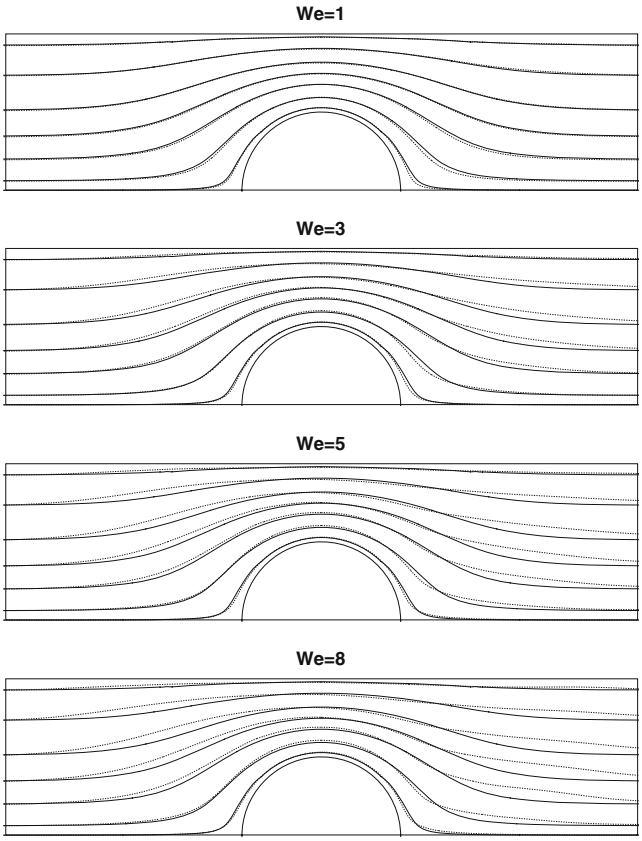

Fig. 10 Comparison of the streamlines for the flow around a cylinder for different Weissenberg numbers using the FENE model. The *solid line* is the Newtonian case and the *dotted line* is for the FENE model for which Re = 0.01, $\beta = 1/9$, and $b = 50$ for $N = 6$ and $N_f = 2{,}000$

decreasing contribution of the stochastic term in Eq. 18. Both steady state and transient values of the drag decrease monotonically with increasing We up to We = 5. Thereafter, there is a slight increase in drag from We = 5 to We = 6. The steady state values of the drag are provided in Table 1. In the inset of Fig. 4d, we plot the evolution of the time-averaged value of the drag given by Eq. 49 for $t \geq 1$, where K_0 is now the smallest integer greater than or equal to $1/\Delta t$. The time-averaged values of the drag clearly decrease as the Weissenberg number is increased up until We = 5, then there is a small increase in drag for We = 6.

A comparison of contours of the components of the polymeric stress and velocity for We = 0.6 and We = 5 is shown in Fig. 5. The contour plots of the velocity components indicate large gradients near the cylinder and the channel wall opposite the cylinder. The peak values of the stress are also to be found in these regions. The axial stress, $\boldsymbol{\tau}_{xx}$, is the dominant stress component and this exhibits stress relaxation as We is increased. On the other hand, the polymeric shear stress increases slightly in concentration in these regions as We is increased from We = 0.6 to We = 5.

In Fig. 6, the evolution of the drag using the Hookean and FENE dumbbell models, and the FENE-P approximation to the FENE model, is compared for We = 0.6, Re = 0.01, $\beta = 1/9$, and $b = 50$ with $N = 6$ and $N_f = 2{,}000$. It can be seen that the steady state values of the drag for the Hookean and FENE (with $b = 50$) dumbbell models are very close, although there is some difference in the transient behavior with the drag for the Hookean dumbbell model lagging behind that for the FENE model. The Oldroyd B model is recovered in the limit as $b \to \infty$ in the FENE model. On the other hand, the initial transient behavior of the drag for the FENE and FENE-P models agree very well. However, at intermediate times, and certainly at steady state, the drag predictions of the two FENE models differ quite significantly for this flow. Therefore, it appears that, for this problem, the FENE-P model is a poor approximation of the FENE model. In the inset of Fig. 6, we plot the evolution of the time-averaged value

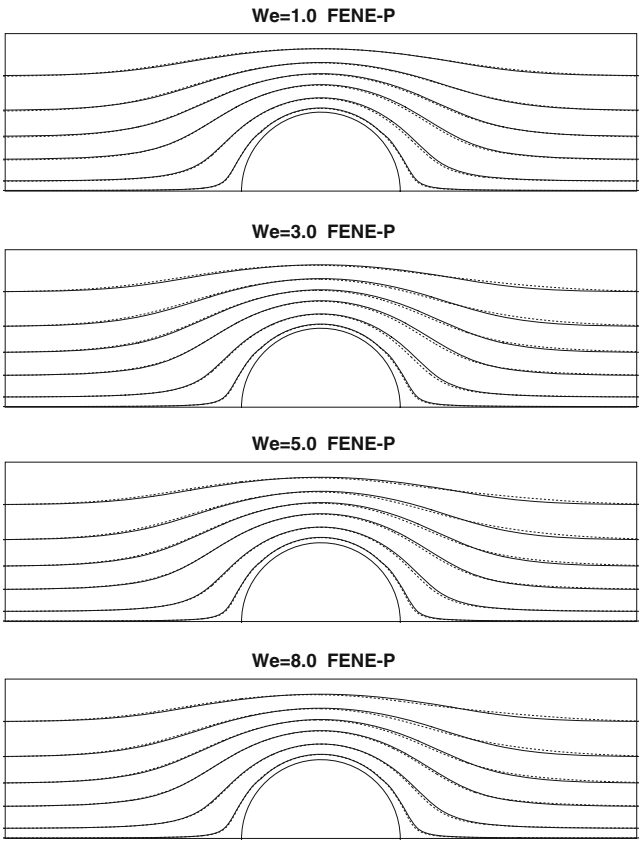

Fig. 11 Comparison of the streamlines for the flow around a cylinder for different Weissenberg numbers using the FENE-P model. The *solid line* is the Newtonian case and the *dotted line* is for the FENE-P model for which Re = 0.01, $\beta = 1/9$, and $b = 50$ for $N = 6$ and $N_f = 2{,}000$

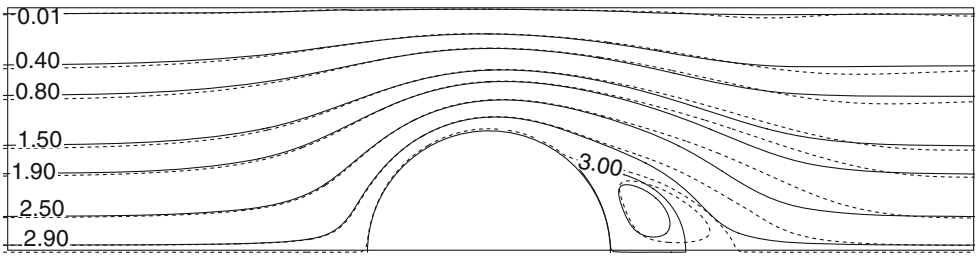

Fig. 12 Comparison of the streamline patterns for We = 0.7 (*solid*) and We = 2 (*dotted*) for the FENE model for which Re = 10, $\beta = 0.59$, and $b = 100$ for $N = 6$ and $N_f = 2{,}000$

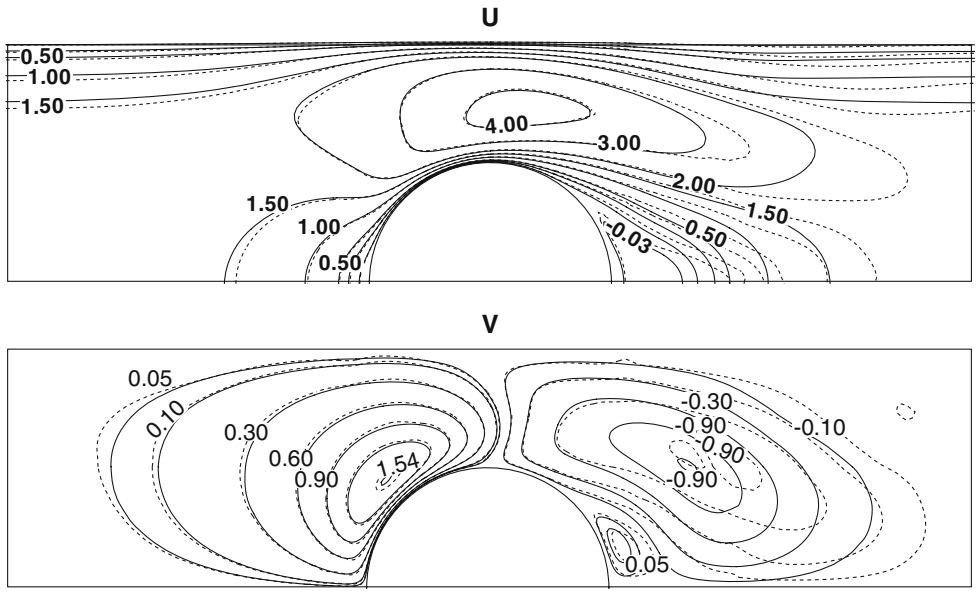

Fig. 13 Comparison of the contours of the velocity components for We = 0.7 (*solid*) and We = 2 (*dotted*) for the FENE model for which Re = 10, $\beta = 0.59$, and $b = 100$ for $N = 6$ and $N_f = 2{,}000$

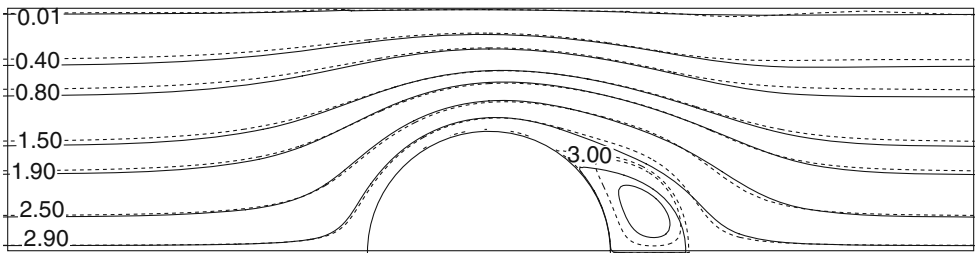

Fig. 14 Comparison of the streamline patterns for Re = 10 (*solid*) and Re = 20 (*dotted*) for the FENE model for which We = 0.7, $\beta = 0.59$, and $b = 100$ for $N = 6$ and $N_f = 2{,}000$

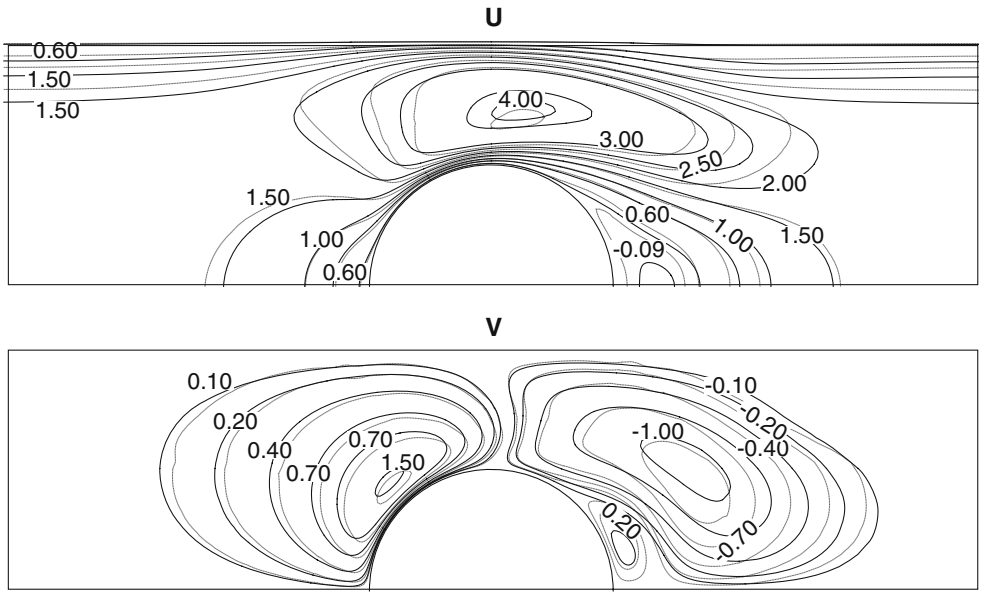

Fig. 15 Comparison of the contours of the velocity components for Re = 10 (*solid*) and Re = 20 (*dotted*) for the FENE model for which We = 0.7, $\beta = 0.59$, and $b = 100$ for $N = 6$ and $N_f = 2{,}000$

Table 2 Dependence of the drag factor, F^*, on N and K for Stokes flow past a sphere

N	K	F^*
6	8	5.9923
7	8	5.9731
8	8	5.9597
9	8	5.9526
10	8	5.9494
5	20	5.9472
6	20	5.9474
7	20	5.9474

of the drag given by Eq. 49 for $t \geq 1$, where K_0 is now the smallest integer greater than or equal to $1/\Delta t$.

The difference in the predictions of the FENE and FENE-P models can be clearly seen in Fig. 7, where the polymeric stress components are plotted around the cylinder and along the downstream axis for Re $= 0.01$, $\beta = 1/9$, $N_f = 2{,}000$, and $b = 50$. The influence of the Weissenberg number on these profiles is shown in this figure. The axial stress component τ_{xx} dominates the other stress components on the surface of the cylinder. From We $= 0.6$, the axial stress starts decreasing with increasing We. This behavior is more accentuated for the FENE-P model than for the FENE model. The maximum value of τ_{xx} in the rear wake remains small in comparison with peak on the cylinder and exhibits little variation with We. Although the FENE-P model provides a good approximation to the FENE model in steady flows, large differences are expected for transient flows (see Herrchen and Öttinger 1997; Keunings 1997, for example). The Peterlin approximation to the FENE model radically changes the statistical properties of the underlying kinetic theory in the sense that the configuration distribution for FENE-P dumbbells is always a Gaussian and, thus, is never localized, irrespective of the flow dynamics (Keunings 1997). A direct consequence of this is that nothing prevents individual FENE-P dumbbells from deforming beyond their maximum extensibility $\sqrt{b}$. It is only the average $\langle \mathbf{Q}^2 \rangle$ that is bounded for FENE-P dumbbells. Therefore, drastic differences between the FENE and FENE-P models are to be expected when simulating complex flows.

The effect of the nondimensional maximum extensibility parameter, b, on the drag on the cylinder and on the stress components is shown in Fig. 8. For smaller values of b, fluctuations of the drag increase, since the molecular chain is small and the tension between the beads is high. However, a smaller value of b makes the chains more rigid, and so, the stresses are higher as observed in Fig. 8. For large values of the maximum extensibility parameter, the behavior of the FENE model approaches that of the Hookean model, as expected.

The effect of the viscosity ratio, β, on the drag on the cylinder and on the polymeric stress components is shown in Fig. 9. Increasing the value of β corresponds to decreasing polymer concentration in the model. The drag increases and the peak values of the polymeric stress components on the cylinder and in the wake in the rear of the cylinder decrease with increasing β.

Turning attention to streamline patterns, Mena and Caswell (1974) presented an analysis for flow of an Oldroyd B fluid past an immersed body by solving the Oseen equations in the far field and matching this solution asymptotically with the Stokes solution near the body. For flow past a cylinder, Mena and Caswell (1974) predicted that the effect of elasticity was to shift the streamlines in the downstream direction. Pilate and Crochet (1977) performed numerical simulations based on a finite difference method using a second-order fluid and found that viscoelasticity reduced the drag coefficient for very low Reynolds numbers, in qualitative agreement with Mena and Caswell (1974). In experimental work on the slow flow of solutions of polyacrylamide in water or in a water-glycerol mixture past a cylinder, Manero and Mena (1981) showed that, for We < 1, the streamlines are shifted downstream, while for We > 1, they are shifted upstream. The streamlines plots of Pilate and Crochet (1977) indicate that elasticity manifests a downstream shift away from the cylinder. In Figs. 10 and 11, we compare the streamline patterns for a Newtonian fluid (Re $= 0.01$) with those of the FENE and FENE-P models (Re $= 0.01$, $\beta = 1/9$) for different Weissenberg numbers from We $= 1$ to We $= 8$. We observe that, for the FENE model at We $= 1$, the streamlines are ever so slightly shifted downstream. On increasing elasticity, the streamlines are shifted in the upstream direction. Using the FENE-P model, the streamlines experience a slight upstream shift, but there is little variation with We, unlike the corresponding behavior for the FENE model.

Increasing Reynolds number

We proceed to evaluate the influence of inertia for the planar flow past a cylinder. Matallah et al. (1998) have

Table 3 Drag factors, F^*, computed by various authors for Stokes flow

Present Paper	5.9474
Lunsmann et al. (1993)	5.9472
Owens and Phillips (1996)	5.9474

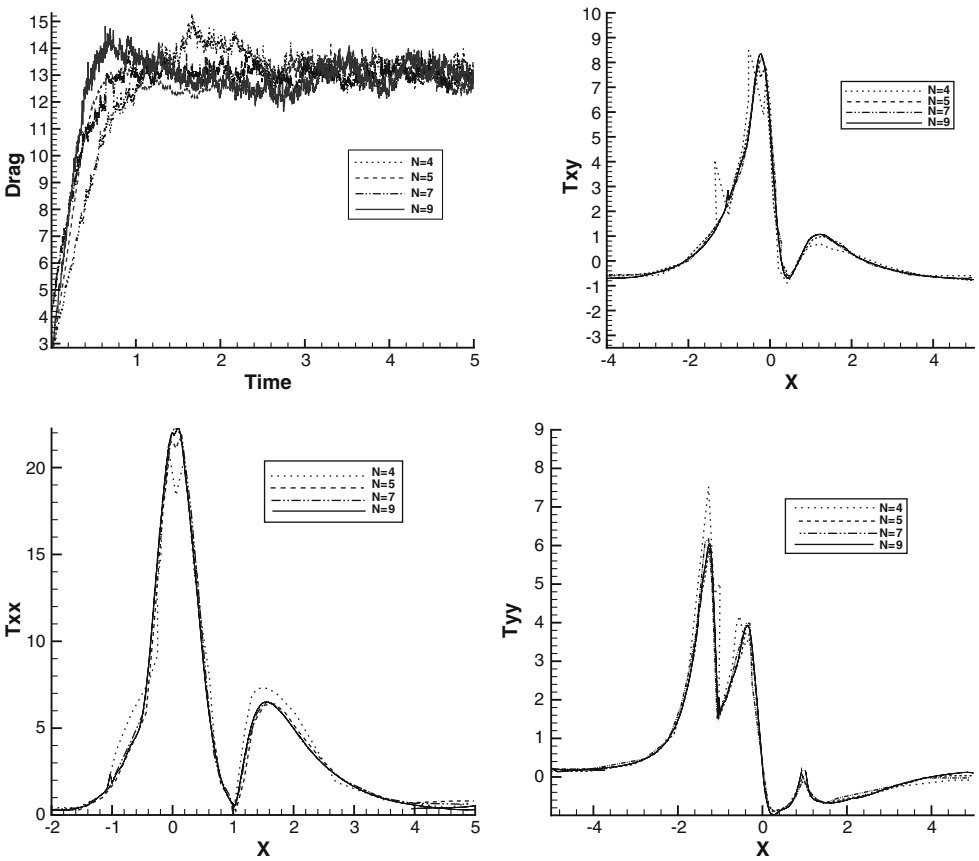

Fig. 16 Dependence of the drag and the polymeric extra-stress components along the center line on polynomial degree for the flow past a sphere for the FENE model for which We = 3, Re = 0.01, $\beta = 1/9$, and $b = 5$ for $N_f = 2{,}000$

performed a numerical study of viscoelastic flow past a cylinder in an unbounded domain. The numerical scheme used a recovery technique in conjunction with a Taylor–Galerkin/pressure correction method with consistent streamline upwinding in order to obtain greater stability at higher Deborah numbers for flow of an Oldroyd B fluid than proved possible using either conventional Taylor–Galerkin (Carew et al. 1993), or EVSS alternatives. By computing flow at Re = 10 past a cylinder, the authors were able to compare the streamlines of their results with those of Townsend (1980) and Pilate and Crochet (1977). Good agreement appeared to be reached, particularly with respect to the downstream shift of the streamlines and the elongated wake behind the cylinder when compared with the Newtonian case. These numerical findings are in general agreement with the experimental results of James and Acosta (1970).

A more recent numerical study has been performed by Hu et al. (2005) using DEVSS-G/SUPG finite element scheme in conjunction with a CONNFFESSIT approach to the microscopic part of the calculation. In order to compare our simulations with those of Hu et al. (2005), the boundary conditions for the velocity at

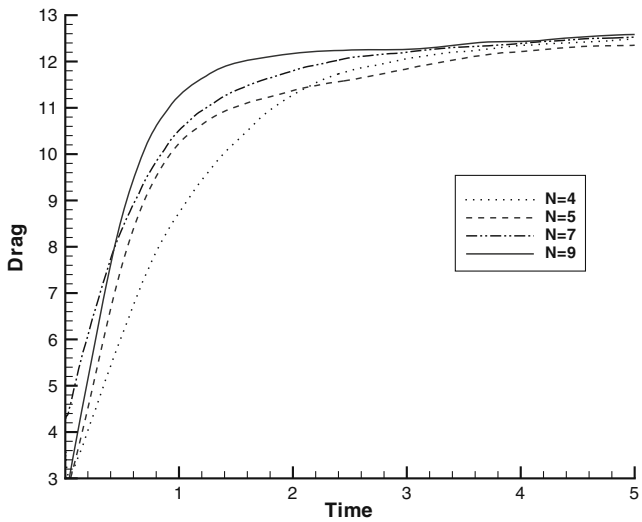

Fig. 17 Comparison of the evolution of the time-averaged drag for the flow past a sphere for the FENE dumbbell as a function of the polynomial degree for We = 3, Re = 0.01, $\beta = 1/9$, and $b = 5$ for $N_f = 2{,}000$

inflow are specified to be $u = 1.5(1 - y^2/4)$, $v = 0$. The material and flow parameters are chosen to be Re = 10, $\beta = 0.59$, and $b = 100$, unless otherwise stated. We compare the streamlines and the velocity components for two different values of elasticity, viz. We = 0.7 and We = 2 in Figs. 12 and 13. The same vortex structure as Hu et al. (2005) is obtained in the wake of the cylinder for We = 0.7. When we increase the elasticity to We = 2, the streamlines and contours of both velocity components shift in the downstream direction. Note that the same contour heights are used in these plots. The recirculation region behind the cylinder increases considerably in the flow direction as We is increased.

When Re is increased from Re = 10 to Re = 20 with We = 0.7, the streamlines shift a little in the upstream direction and the vortex increases its size in the normal direction to the flow, as can be seen in Fig. 14, causing the position of the separation point at the rear of the cylinder to move away from the axis of symmetry. For nonzero values of the Reynolds number, the convection effect propagates from upstream to downstream. The velocity patterns shift downstream when the Reynolds number is increased to Re = 10 from Re = 0.01. There is little change when the Reynolds number is further increased to Re = 20 (see Fig. 15).

Flow past a sphere

Stokes flow

As a precursor to the consideration of the flow of a FENE model fluid past a sphere in a cylinder, the Stokes problem is solved to validate the extension of the method to axisymmetric flows. The numerical results are compared with those in the literature. Note that the Stokes problem can be solved without recourse to the transient algorithm by simply solving the steady problem.

The drag is determined by integrating the total stress over the surface of the sphere. The drag on the sphere, F, is given by

$$F = -2\pi a^2 \int_0^{\pi} \left\{ \left(-p + 2\beta \frac{\partial u}{\partial z} + \tau_{zz} \right) \cos\theta + \left(\beta \left(\frac{\partial v}{\partial z} + \frac{\partial u}{\partial r} \right) + \tau_{rz} \right) \sin\theta \right\} \sin\theta \, d\theta, \tag{50}$$

where u and v are the components of the velocity in the axial and radial directions, respectively. The quantity

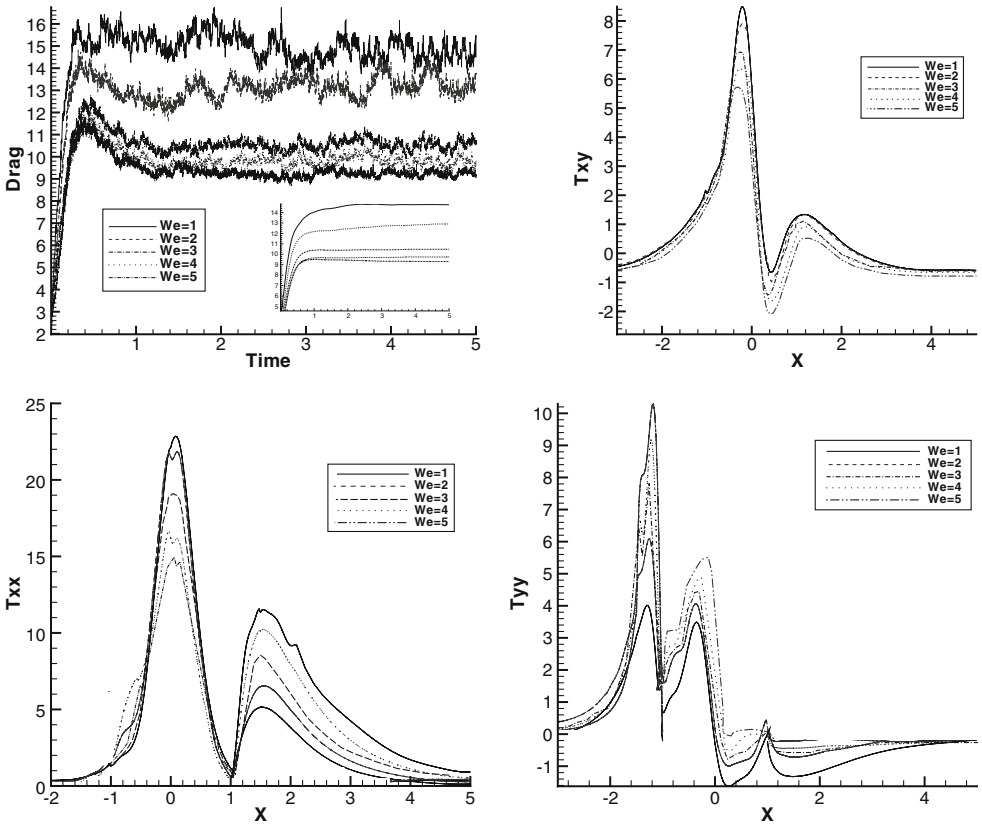

Fig. 18 Dependence of the drag and the polymeric extra-stress components along the center line on Weissenberg number for the flow past a sphere for the FENE model for which Re = 0.01, $\beta = 1/9$, and $b = 5$ for $N = 6$ and $N_f = 2{,}000$

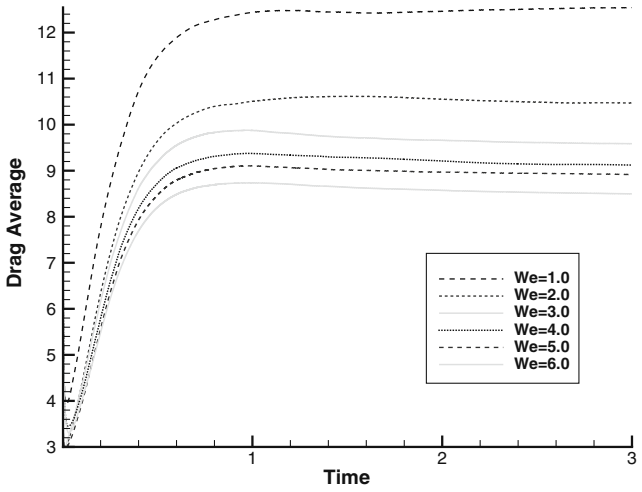

Fig. 19 Comparison of the evolution of the time-averaged drag for the flow past a sphere for the FENE dumbbell as a function of the Weissenberg number for Re = 0.01, $\beta = 1/9$, and $b = 5$ for $N = 6$ and $N_f = 2{,}000$

that is generally used to compare numerical solutions against each other is the drag factor F^* defined as the ratio of the drag experienced by a sphere to the drag that would be experienced by the same sphere in an infinite expanse of Newtonian fluid, and is given by the formula

$$F^* = \frac{F}{6\pi\eta U a} \tag{51}$$

Table 2 shows the convergence behavior of the drag on the sphere surface as the order of polynomial approximation N is increased for $K = 8$ and $K = 20$. The value of the drag factor F^* computed using the spectral element method was $F^* = 5.9474$ when the discretization parameters were chosen to be $K = 20$ and $N = 7$. This is in excellent agreement with the predictions of Lunsmann et al. (1993) and Owens and Phillips (1996) as shown in Table 3.

FENE model

In the last part of this work, the numerical scheme extended to treat axisymmetric flow problems is applied to the problem of viscoelastic flow past a sphere in a cylinder using the FENE model. Convergence with mesh refinement is demonstrated for We = 3, Re = 0.01, $\beta = 1/9$, and $b = 5$. In all cases, the number of configuration fields is fixed at $N_f = 2{,}000$. The velocity field at inflow corresponds to uniform flow, i.e., $u = 1$, $v = 0$. The evolution of the drag and the components of the polymeric contribution to the extra-stress tensor around the sphere and along the downstream axis are shown in Fig. 16 as a function of the order of polynomial approximation, N. The evolution of the time-averaged drag is shown in Fig. 17. These plots show that, although there is very little difference in the time-averaged drag, which seems to have converged for low-order polynomial approximations, there is great variation in the

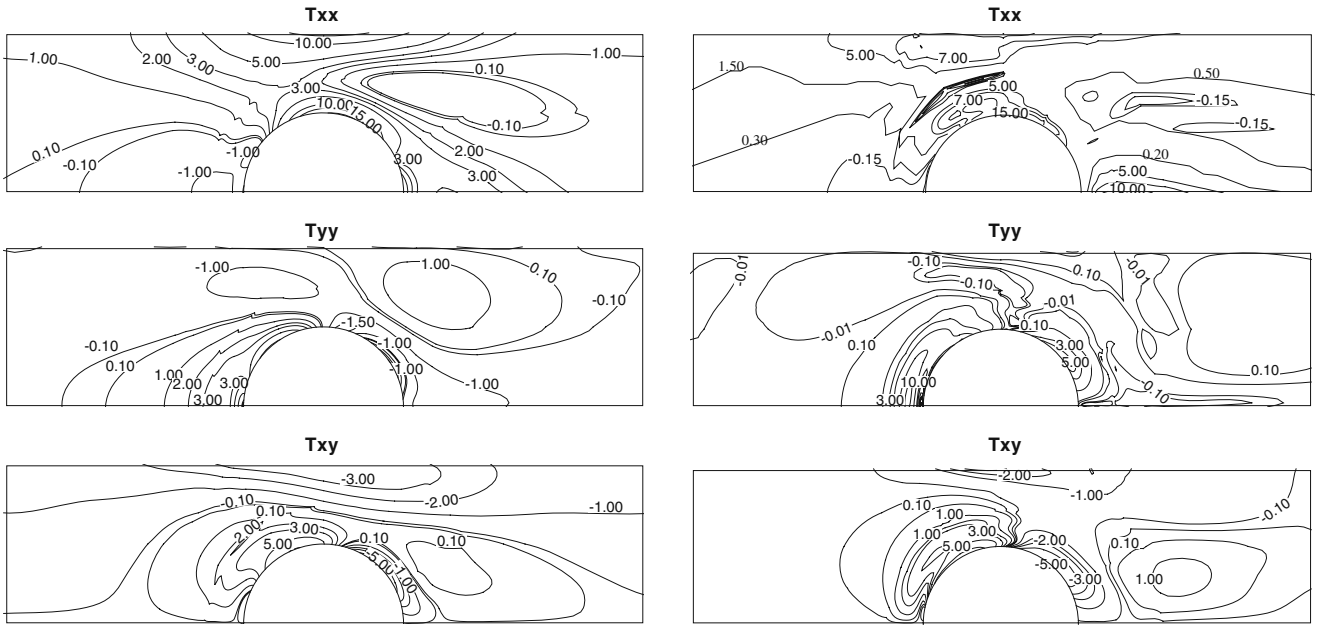

Fig. 20 Comparison of the contour plots of the stress components generated using the FENE model for flow past a sphere for We = 1 (*left*) and We = 5 (*right*) for Re = 0.01, $\beta = 1/9$, and $b = 5$ with $N = 6$ and $N_f = 2{,}000$

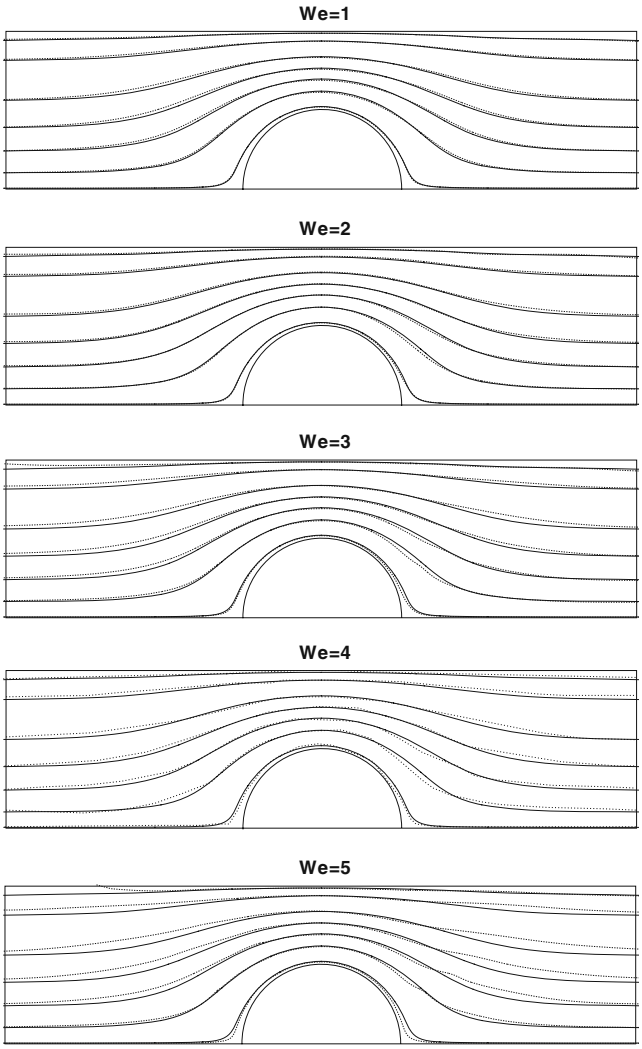

Fig. 21 Comparison of the streamline patterns for the flow around a sphere for different Weissenberg numbers: Newtonian (*solid*) and FENE (*dotted*) with Re = 0.01, $\beta = 1/9$, and $b = 5$ for $N = 6$ and $N_f = 2{,}000$

profiles of the stress components around the cylinder and along the center line. In particular, τ_{xx} is underpredicted and τ_{yy} is vastly overpredicted on the sphere itself when N is too small. Clearly, too coarse a mesh fails to provide accurate predictions of these quantities even though the drag appears to have converged. However, there is very little difference between the predictions with $N = 7$ and $N = 9$ even in the peak values of the stress components on and downstream of the sphere. These figures show that, even though the steady state value of the time-averaged drag appears to be the same for all values of N, the variation in the corresponding fields can be large if sufficient mesh refinement has not been performed.

In Fig. 18, we show the influence of the Weissenberg number on the evolution of the drag and the components of the polymeric contribution to the extra-stress tensor around the sphere and along the downstream axis. There is drag reduction and stress relaxation as the Weissenberg number is increased. This behavior is similar to that observed in the corresponding cylinder problem. The evolution of the time-averaged drag is shown in Fig. 19. After the initial evolution, the time-averaged drag settles down to its steady state value just after $t = 1$. The influence of elasticity on the contours of the components of the polymeric contribution of the extra-stress tensor is shown in Fig. 20. In this figure, the contours of the stress components are displayed for We = 1 and We = 5. The normal stress component τ_{xx} and the shear stress τ_{xy} relax with increasing Weissenberg number. The normal stress component τ_{yy} initially relaxes before increasing again from We = 3.

Finally, the influence of elasticity on the streamlines is shown in Fig. 21. An upstream shift in the streamlines is observed as We is increased.

Conclusions

In this paper, a spectral element method has been presented for performing numerical simulations of dilute polymer solutions using the method of Brownian configuration fields. The numerical method has been used to predict the viscoelastic flow past a cylinder using the Hookean, FENE, and FENE-P dumbbell models. The method of Brownian configuration fields based on Hookean dumbbells was validated by comparing predictions with those obtained using a macroscopic method based on the mathematically equivalent Oldroyd B model. Excellent agreement was obtained between the two distinct but equivalent modelling approaches.

The method was then used to perform an extensive set of calculations for the FENE model in which convergence with mesh refinement was investigated with respect to the order of polynomial approximation and the number of configuration fields used for the stochastic part of the calculation. The influence of the Weissenberg number, Reynolds number, finite extensibility parameter and the viscosity ratio on the drag, and the profiles of the polymeric contribution of the extra stress around the cylinder and along the axis of symmetry is investigated. The drag decreases with increasing Weissenberg number since the increasing domination of shear over extension around the cylinder causes the stress to relax with increasing Weissenberg number. Increasing the finite extensibility parameter has a negligible effect on the steady state value of the

drag, but there are large differences in the transient development to steady state. Increasing the viscosity ratio, β, diminishes the drag since the stress components are substantially reduced as $\beta \to 1$. There is an upstream shift in the streamlines as the Weissenberg number increases for the FENE model.

It is also shown that there are large differences between the FENE model and one of its closure approximations, the FENE-P model, in terms of the predictions of the polymeric stress components along the axis of symmetry and around the cylinder. The differences along the axis of symmetry are to be expected since the flow has a large extensional component and the FENE-P model is known to provide a poor approximation to the FENE model in extensional-dominated flows.

The numerical algorithm was modified for use in axisymmetric flows in order to investigate the flow of a FENE model fluid around a sphere in a cylinder. As with the cylinder problem, it is shown that stress relaxes around the sphere as the Weissenberg number increases, causing a decrease in the drag. The streamlines exhibit an initial downstream shift with increasing Weissenberg number, followed by a subsequent upstream shift as the Weissenberg number is increased further.

Acknowledgements The first author would like to acknowledge the financial support from the National Council for Science and Technology (CONACYT) of Mexico and also to Project 47192 for funding his doctoral studies at UNAM. Part of this work was performed while the first author was a visiting postgraduate researcher at Cardiff University.

References

Bird RB, Curtiss CF, Armstrong RC, Hassager O (1987) Dynamics of polymeric liquids, vol. 2. Wiley, New York

Carew EOA, Townsend P, Webster MF (1993) A Taylor-Petrov-Galerkin algorithm for viscoelastic flow. J Non-Newton Fluid Mech 50:253–287

Chauvière C, Lozinski A (2008) Simulation of dilute polymer solutions using a Fokker–Planck equation. Comput Fluids 33:687–696

Feigl K, Laso M, Öttinger HC (1995) CONNFFESSIT approach for solving a two-dimensional viscoelastic flow problem. Macromol 28:3261–3274

Gerritsma MI, Phillips TN (2000) Spectral element methods for axisymmetric stokes problems. J Comput Phys 164:81–103

Gordon WJ, Hall CA (1973) Construction of curvilinear coordinate systems and application to mesh generation. Int J Numer Methods Fluids 7:461–477

Halin P, Lielens G, Keunings R, Legat V (1998) The Lagrangian particle method for macroscopic and micro–macro viscoelastic flow computations. J Non-Newton Fluid Mech 79: 387–403

Herrchen M, Öttinger H-C (1997) A detailed comparison of various FENE dumbbell models. J Non-Newton Fluid Mech 68:17–42

Hu X, Ding Z, Lee LJ (2005) Simulation of 2d transient viscoelastic flow using the CONNFFESSIT approach. J Non-Newton Fluid Mech 127:107–122

Hua CC, Schieber JD (1998) Viscoelastic flow through fibrous media using the CONNFFESSIT approach. J Rheol 42: 477–491

Hulsen MA, van Heel APG, van den Brule BHAA (1997) Simulation of viscoelastic flows using Brownian configuration fields. J Non-Newton Fluid Mech 70:79–101

Inkson NJ, Phillips TN, van Os RGM (2008) Numerical simulation of flow past a cylinder using models of XPP type. J Non-Newton Fluid Mech xx:xx

James DF, Acosta AJ (1970) On the slow flow of viscoelastic liquids past a circular cylinder. J Non-Newton Fluid Mech 42:269–288

Karniadakis GEM, Sherwin SJ (1999) Spectral/hp element methods for CFD. Oxford University Press, Oxford

Keunings R (1997) On the Peterlin approximation for finitely extensible dumbbells. J Non-Newton Fluid Mech 68: 85–100

Kröger M, Ammar A, Chinesta F (2008) Consistent closure schemes for statistical models of anisotropic fluids. J Non-Newton Fluid Mech 149:40–55

Laso M, Öttinger HC (1993) Calculation of viscoelastic flow using molecular models: the CONNFFESSIT approch. J Non-Newton Fluid Mech 47:1–20

Lielens G, Keunings R, Legat V (1999) The FENE-L and FENE-LS closure approximations to the kinetic theory of finitely extensible dumbbells. J Non-Newton Fluid Mech 87: 179–196

Lozinski A, Chauvière C, Fang J, Owens RG (2003) A Fokker-Planck simulation of fast flows of concentrated polymer solutions in complex geometries. J Rheol 47:535–561

Lunsmann WJ, Genieser L, Armstrong RC, Brown RA (1993) Finite element analysis of steady viscoelastic flow around a sphere in a tube: calculations with constant viscosity models. J Non-Newton Fluid Mech 48:63–99

Maday Y, Patera AT (1989) Spectral element methods for the incompressible Navier–Stokes equations. In: Noor AK, Oden JT (eds) State of the art surveys in computational mechanics. ASME, New York, pp 71–143

Manero O, Mena B (1981) On the slow flow of viscoelastic liquids past a circular cylinder. J Non-Newton Fluid Mech 9: 379–387

Matallah H, Townsend P, Webster MF (1998) Recovery and stress splitting schemes for viscoelastic flows. J Non-Newton Fluid Mech 75:139–166

McLeish TCB, Larson RG (1998) Molecular constitutive equations for a class of branched polymers: the pom-pom polymer. J Rheol 42:81–110

Melchior M, Öttinger H-C (1995) Variance reduced simulations of stochastic differential equations. J Chem Phys 103:9506–9509

Melchior M, Öttinger H-C (1996) Variance reduced simulations of polymer dynamics. J Chem Phys 105:3316–3331

Mena B, Caswell B (1974) Slow flow of an elastic-viscous fluid past an immersed body. Chem Eng J 8:125–134

Orszag SA (1980) Spectral methods for problems in complex geometries. J Comput Phys 37:70–92

Öttinger H-C (1996) Stochastic processes in polymeric fluids: tools and examples for developing simulation algorithms. Springer, Berlin

Öttinger H-C, van den Brule BHAA, Hulsen MA (1997) Brownian configuration fields and variance reduced CONNFFESSIT. J Non-Newton Fluid Mech 70:255–261

Owens RG, Phillips TN (1996) Steady viscoelastic flow past a sphere using spectral elements. Int J Numer Methods Eng 39:1517–1534

Owens RG, Phillips TN (2002) Computational rheology. Imperial College Press, London

Patera AT (1984) A spectral element method for fluid dynamics: laminar flow in a channel expansion. J Comput Phys 54: 468–488

Peterlin A (1966) Hydrodynamics of macromolecules in a velocity field with longitudinal gradient. J Polym Sci B 4:287–291

Phillips TN, Smith KD (2006) A spectral element approach to the simulation of viscoelastic flows using Brownian configuration fields. J Non-Newton Fluid Mech 138:98–110

Pilate G, Crochet MJ (1977) On the slow flow of viscoelastic liquids past a circular cylinder. J Non-Newton Fluid Mech 2:323–341

Sizaire R, Lielens G, Jaumain I, Keunings R, Legat V (1999) On the hysteretic behaviour of dilute polymer solutions in relaxation following extensional flow. J Non-Newton Fluid Mech 82:233–253

Townsend P (1980) A numerical simulation of Newtonian and visco-elastic flow past stationary and rotating cylinders. J Non-Newton Fluid Mech 6:219–243

Verbeeten WMH, Peters GWM, Baaijens FTP (2001) Differential constitutive equations for polymer melts: the extended pom-pom model. J Rheol 45(4):823–843

Verbeeten WMH, Peters GWM, Baaijens FTP (2002) Viscoelastic analysis of complex melt flows using the extended pom-pom model. J Non-Newton Fluid Mech 108:301–326